Time-Domain Reflectometry Measurements and Modelling of Firn Meltwater Infiltration at DYE-2, Greenland

S. Samimi[1], S. J. Marshall[1,2], B. Vandecrux[3] and M. MacFerrin[4]

[1]Department of Geography, University of Calgary, Calgary, Alberta, Canada.

[2]Environment and Climate Change Canada, Gatineau, Quebec, Canada.

[3]Geological Survey of Denmark and Greenland, Copenhagen, Denmark.

[4]CIRES Institute, University of Colorado, Boulder, Colorado, USA.

Corresponding author: Samira Samimi (samira.samimi@ucalgary.ca)

Key Points:

- Time-domain reflectometry provided continuous monitoring of firn liquid water content and meltwater infiltration through a melt season
- A simple coupled model of firn thermodynamics and hydrology reproduces the observed evolution of the firn thawing and wetting fronts
- Modeling from 1950-2020 indicates that extreme melt seasons govern trends in firn temperature, density, and ice content at DYE-2

Abstract

Meltwater infiltration and refreezing in snow and firn are important processes for Greenland Ice Sheet mass balance, acting to reduce meltwater runoff and mass loss. To advance understanding of meltwater retention processes in firn, we deployed vertical arrays of time-domain reflectometry sensors and thermistors to continuously monitor meltwater infiltration, refreezing, and wetting-front propagation in the upper 4 m of snow and firn over the 2016 melt season at DYE-2, Greenland. The dataset provides a detailed record of the co-development of the firn wetting and thawing fronts through the melt season. These data are used to constrain a model of firn thermodynamics and hydrology that is then used in simulations of the long-term firn evolution at DYE-2, forced by ERA5 climate reanalyses over the period 1950-2020. Summer 2016 meltwater infiltration reached a depth of 1.8 m below the surface, which is close to the modelled long-term mean at this site. Modelled meltwater infiltration increased at DYE-2 from 1990-2020, driving increases in firn density, ice content, and temperature; 10-m firn temperatures increased by 1°C per decade over this period. Modelled meltwater infiltration reached 6 to 7 m depth during extreme melt seasons in Greenland such as 2012 and 2019, causing 3-4°C increases in 10-m firn temperatures which persist for several years. A similar event occurred in 1968 in the model reconstructions. These deep infiltration events strongly impact the firn at DYE-2, and may be more influential than the background warming trend in governing meltwater retention capacity in the Greenland percolation zone.

Plain Language Summary

Meltwater on ice sheets can be retained within the system if it infiltrates the firn and refreezes. This is an important mass balance process for the Greenland Ice Sheet, reducing meltwater runoff and associated sea-level rise. The processes of meltwater infiltration and refreezing are not fully understood, however, and are difficult to remotely monitor. We deployed vertical arrays of thermistors and time-domain reflectometry (TDR) probes to 4 m depth in the firn to continuously monitor meltwater infiltration and refeezing processes through a summer melt season at DYE-2, Greenland. The observations provide a detailed picture of the coupled thermal and hydrological evolution of the firn through the 2016 melt season, including estimates of firn

water content. The thaw and wetting fronts reached a maximum depth of 1.8 m, with meltwater infiltration concentrated in four main pulses of melting and subsurface warming that reached progressively deeper into the firn. The observations were used to constrain a coupled model of firn thermodynamics and hydrology, which was then run over the period 1950-2020, driven by meteorological forcing from ERA5 climate reanalyses. The model results suggest that decadal-scale firn evolution at DYE-2 is strongly influenced by extreme melt seasons such as those of 1968, 2012, and 2019, when meltwater infiltration reached depths of 6-7 m. Extreme melt years drive increases in firn temperature, ice content, and density, reducing firn meltwater retention capacity. Such processes are likely to govern future meltwater retention as the percolation zone extends to higher elevations in Greenland in the coming decades.

1 Introduction

In the accumulation area of the Greenland Ice Sheet, meltwater percolates into the underlying seasonal snow and firn, where it can refreeze (Benson, 1962; Pfeffer et al., 1991; Braithwaite et al., 1994). Meltwater retention from this process is well-documented in the Greenland percolation zone, and it is a critical mass balance process with the potential to buffer sea level rise associated with ice sheet melt (Harper et al., 2012; Rennerhalm et al., 2013). Meltwater infiltration and refreezing are expected to increase in importance as the Greenland Ice Sheet percolation zone expands to higher elevations in a warming world (van Angelen et al., 2013; Noël et al., 2017; MacFerrin et al., 2019).

Meltwater that percolates and refreezes is difficult to account for in altimetric measurements of surface mass balance, as it is not possible to observe how much meltwater is retained within the system (Sørensen et al., 2011; Kuipers Munneke et al., 2015). Meltwater retention is also a source of uncertainty in mass balance models in Greenland, due to the complexities of meltwater infiltration and ice layer formation processes (e.g., Reijmer et al., 2012; Vernon et al., 2013, Steger et al., 2017a, Langen et al., 2017). Processes of meltwater percolation and refreezing occur at fine scales, are spatially heterogeneous, and *in situ* observations are scarce (Humphrey et al., 2012; van As et al., 2016). This makes it difficult to calibrate and validate snow and firn models, particularly on the scale of polar ice caps and ice sheets (Steger et al., 2017b; Verjans et al., 2019; Vandecrux et al., 2020b).

Meltwater percolation in snow can take the form of relatively homogeneous infiltration (e.g., Marsh and Woo, 1984) or vertical 'piping' of water, via preferential flow pathways (Marsh and Woo, 1984; Williams et al. 2010; Pfeffer and Humphrey, 1998; Humphrey et al., 2012). Meltwater may percolate to a certain depth before it reaches an impermeable ice layer or refreezes (e.g., Cobeck, 1979). Subsurface grain size, density, or permeability contrasts can cause meltwater to spread horizontally, leading to the development of ice layers (Katsushima et al., 2013, Avanzi et al., 2016). With sufficient melt, individual ice lenses can merge into thick, horizontally-extensive ice layers, which inhibit meltwater percolation (Gascon et al., 2013; de la Peña et al., 2015; Machguth et al., 2016, MacFerrin et al., 2019).

At high elevations in the Greenland Ice Sheet percolation zone, cooler temperatures and lower melt rates result in greater near-surface pore space, cold content, and hydraulic permeability, promoting meltwater retention (Verjans et al., 2019; Vandecrux et al., 2020a). Where melting is moderate, ice lenses and layers are typically discontinuous over horizontal length scales of less than 1 m (e.g., Parry et al., 2007; Dunse et al., 2008). There is evidence that meltwater can effectively infiltrate ice-rich firn in this environment (Machguth et al., 2016), including ice layers that are up to ~0.1 m thick (Samimi et al., 2020). However, climate warming is expected to cause increases in firn temperature, density, and near-surface ice layers in the upper percolation zone of the ice sheet in the coming decades (van Angelen et al., 2013; de la Peña et al., 2015; Noël et al., 2017; MacFerrin et al., 2019), reducing meltwater retention capacity and potentially driving a transition from meltwater retention to runoff.

To advance understanding of meltwater infiltration processes in the Greenland percolation zone, we designed field experiments at DYE-2 in southwest Greenland to continuously monitor the coupled thermal and hydrological evolution in the near-surface firn. Vertical arrays of thermistors and time-domain-reflectometry (TDR) sensors were deployed to 4.3 m depth to track meltwater infiltration through the 2016 melt season. The thermistor arrays monitor firn temperature and the latent heat signature of meltwater refreezing (e.g., Humphrey et al., 2012; Charalampidis et al., 2016). TDR probes provide additional information because the dielectric permittivity of snow and firn is strongly sensitive to small amounts of liquid meltwater (Schneebeli et al., 1997; Techel and Pielmeier, 2011). The dielectric permittivity therefore provides a measure of liquid water content and arrays of TDR probes can directly track the seasonal evolution of the wetting front, in conjunction with its thermal signature. Samimi and Marshall (2017) successfully deployed TDR sensors for this purpose in a mountain glacier setting. In the current study we extend this work to polar snow and firn, where temperatures and liquid water content are lower but meltwater refreezing is a more significant process.

Sensors were installed in two firn pits at DYE-2 in spring 2016 and left in place until spring 2017. Samimi et al. (2020) present initial results from this study, including evidence of meltwater percolation through ice layers in the near-surface firn. Here we present the detailed

thermistor and TDR records through the 2016 melt season, including estimates of the liquid water content and effective hydraulic conductivity of the snow and firn. The observations are used to constrain and tune a multi-layer model which simulates the coupled subsurface hydrological and thermal evolution in the upper 20 m of snow and firn. This model is then run through the historical period 1997-2018 for which GC-Net Automatic Weather Station (AWS) data are available at DYE-2 (Steffen and Box, 2001), to place the 2016 melt season in context. We further extend the firn simulations to the period 1950-2020 using bias-adjusted meteorological forcing from ERA5 climate reanalysis (Hersbach et al., 2020).

Increased melt rates in Greenland are expected to drive increases in firn temperature, density, and ice content, which will decrease meltwater storage capacity (de la Peña et al., 2015; Machguth et al., 2016; Vandecrux et al., 2020a). Future projections of Greenland Ice Sheet response to climate warming and associated sea-level rise require a quantitative understanding of these processes. It is uncertain whether firn evolution is more sensitive to long-term warming (e.g., Hanna et al., 2012, 2021) or the impacts of extreme melt seasons such as those witnessed in 2012 and 2019 (Nghiem et al., 2012; Hanna et al., 2014; Tedesco and Fettweis, 2020). These extreme melt seasons were associated with strong anticyclonic conditions that persisted for days to weeks (Fettweis et al., 2013; Hanna et al., 2014; Rajewicz and Marshall, 2014), causing anomalous melt which extended to high elevations of the ice sheet in both 2012 (Nghiem et al., 2012) and 2019 (Tedesco and Fettweis, 2020). Large amounts of meltwater during such events can create thick near-surface ice slabs (Machguth et al., 2016; Noël et al., 2017) or drive deep meltwater infiltration, firn warming, and densification, with associated reductions in meltwater retention capacity. We use the calibrated firn model to examine the historical frequency of extreme melt events since 1950, their impacts on the firn, and the significance of such events in comparison with the long-term climate and firn evolution.

2 Study Site and Research Methods

2.1 DYE-2, Greenland

Our field study was part of the FirnCover project, which aimed to increase understanding of firn densification and meltwater retention processes in the Greenland Ice Sheet percolation zone

(Machguth et al., 2016; MacFerrin et al., 2019). In April, 2016 we established observation sites in the near-surface firn at 66˚28′39″N, 46˚17′5″W, near DYE-2 station on the southwestern flank of the ice sheet (Figure 1). The study sites were at an elevation of 2120 m, in the upper part of the percolation zone of southwestern Greenland. Summer melt in this zone is retained through meltwater refreezing, but commonly infiltrates beyond the annual snow layer (Benson, 1962). DYE-2 has a slope of less than 1° and there is no evidence of surface water ponding or horizontal surface water flow.

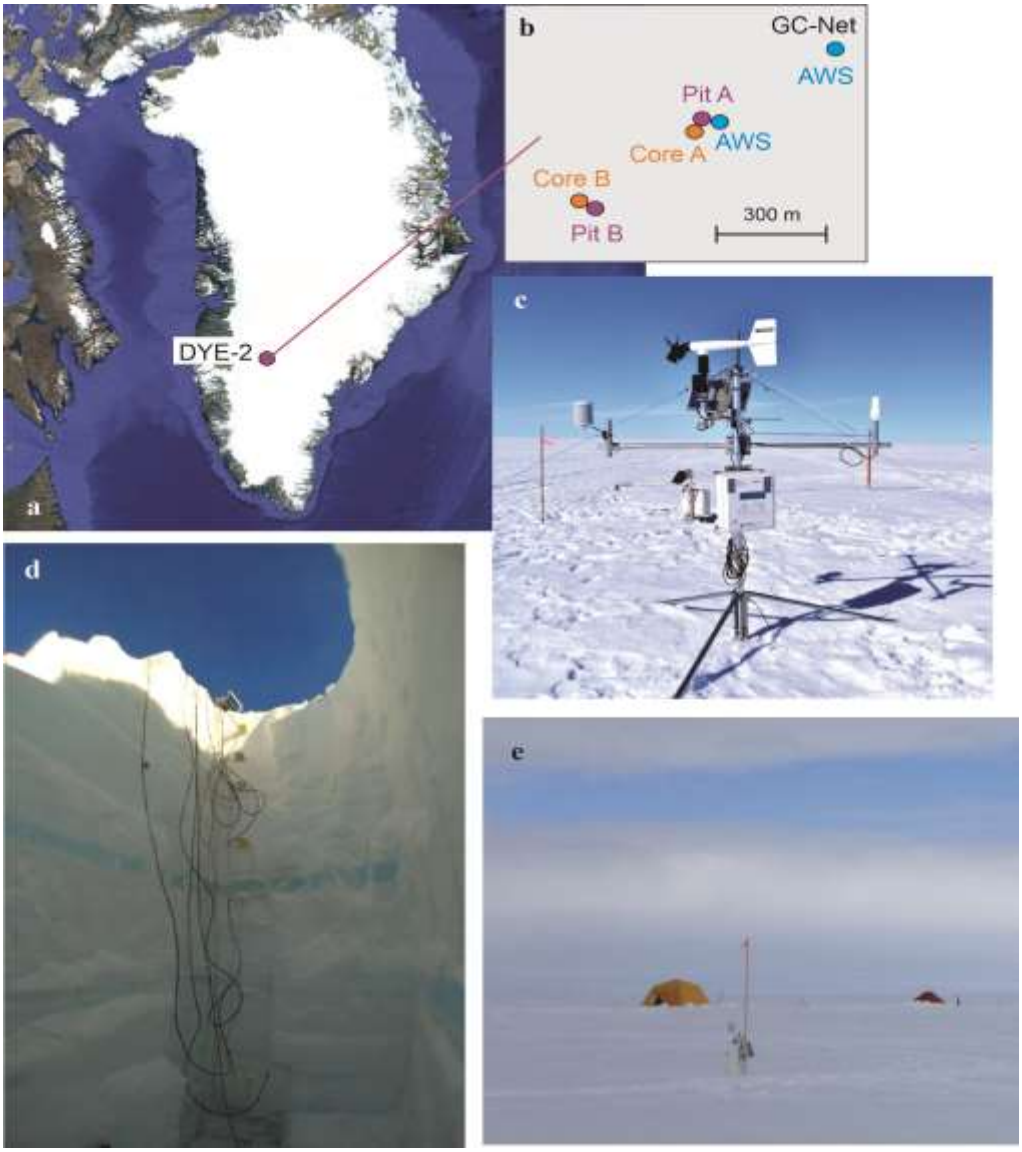

Figure 1. (a,b) Study area at DYE-2, Greenland, indicating the firn pit and AWS locations. (c) AWS at site A. (d) The upper part of firn pit A showing the TDR sensors and examples of ice layers at this site, prior to filling in the pit. (e) Firn pit B after filling it in (foreground, with the datalogger box, UDG, and temperature sensor).

A 100.2-m ice core collected at DYE-2 in 1977 indicates a mean annual accumulation rate of 0.34 m w.e. yr^{-1} for the period ~1740 to 1976 (Clausen et al., 1988; Shoji et al., 1991). This has increased by about 10% in recent decades, as firn cores at DYE-2 acquired by Ohio State University (OSU) in 1998 indicate a mean annual accumulation of 0.365 mm w.e. yr^{-1} for the period 1969-1998 (Mosley-Thompson et al., 2001). From 2013 to 2016, shallow firn cores were drilled each year by FirnCover project participants at DYE-2. Machguth et al. (2016) analyzed the 2013 and 2015 firn density and stratigraphy and compared their results with the 1998 OSU ice cores. From 1998 to 2013, density increased by ~140 kg m^{-3} in the top 7 meter of firn and ~100 kg m^{-3} from 8 to 16 m depth. The increases in density are associated with higher ice content (i.e., increases in refrozen meltwater), and meltwater penetration heavily modified the pre-1998 firn stratigraphy recorded by Mosley-Thompson et al. (2001). The Machguth et al. (2016) study indicates that DYE-2 may be undergoing a transition to denser and more ice-rich firn, characteristic of the lower percolation zone.

Our study sites were within 1 km of the Greenland Climate network (GC-Net) automatic weather station established at DYE-2 in 1996 (66˚28′50″N, 46˚16′59″W; Steffen and Box, 2001). Mean annual and mean summer (June through August, or JJA) 2-m air temperatures at the GC-Net station were T_{ann} = –17.4°C and T_{JJA} = –5.4°C from 1997 to 2018. Based on the GC-Net data, the melt season at DYE-2 typically runs from mid-June to mid-August. DYE-2 experiences an average of 28 melt days each summer (JJA), as calculated from days with maximum hourly air temperatures exceeding 0°C. Annual positive degree days (*PDD*) at the site averaged 8.6°C·d from 1997-2018. For the period 1997-2000, Steffen and Box (2001) report a mean annual air temperature of –18.9°C at DYE-2 and a 10-m firn temperature of –16.5°C. Firn temperatures at 10-m depth are warmer than the mean annual air temperature due to latent heat release from refreezing meltwater.

There is evidence of firn warming at DYE-2 over the last four decades. Clausen et al. (1988) report a 10-m firn temperature of –17.2°C at DYE-2, based on measurements made during the 1977 ice-coring campaign. This warmed to about –16.5°C in the late 1990s (Steffen and Box (2001), and GC-Net thermistor measurements at DYE-2 indicate an additional ~1.5°C of warming from 1998 to 2009, to a 10-m temperature of –15°C. Consistent with this, Vandecrux et

al. (2020a) report a warming of 1.1°C per decade at 10-m depth at DYE-2, based on firn modelling over the period 1998-2018. Firn warming exceeds atmospheric warming over this period, indicating an increase in meltwater production and refreezing at this site.

DYE-2 appears to have remained within the accumulation area of the ice sheet for the entire period of GC-Net observations, with seasonal snow persisting each year, although the end-of-summer snowline (ELA) advanced near to this elevation in 2012, the warmest summer on record. DYE-2 experienced 66 melt days in 2012, with a mean summer temperature T_{JJA} = –2.9°C and *PDD* totals of 37.2°C·d. The mean JJA surface albedo in 2012 was 0.73, lower than normal (0.79) but diagnostic of persistent snow cover. The heavy melt season of summer 2012 may account for much of the deep meltwater infiltration, increased ice content, and densification recorded by Machguth et al. (2016) in the 2013 firn core, relative to the 1998 OSU cores.

Specific to the period of study discussed in this manuscript, the summer of 2016 was 0.8°C warmer than mean conditions from 1997-2018, with T_{JJA} = –4.6°C and a total of 37 melt days. The winter snowpack was ~0.9 m deep in mid-April of 2016, representing an accumulation of 325 mm w.e. In addition to our TDR experiments to monitor meltwater infiltration through the summer 2016 melt season, Heilig et al. (2018) installed an upward-looking ground-penetrating radar system at 4.3 m depth to monitor the evolution of the wetting front and the snow/firn liquid water content. The radar measurements indicate a total melt of ~0.15 m w.e. at DYE-2 in the summer of 2016 (Heilig et al., 2018). Of this, about 0.09 m w.e. (60%) refroze within the seasonal snowpack and 0.06 m w.e. (40%) infiltrated the firn, with a maximum meltwater infiltration depth of 2.3 m below the surface.

2.2 Firn Measurements and TDR Methods

2.2.1 Thermistor and TDR Measurements

We established TDR and thermistor arrays at two locations near DYE-2 in April, 2016, excavating firn pits to depths of 2.2 and 5.3 m (Figure 1). The two sites, referred to as A and B, are 400 m apart (Figure 1b). The 2015-2016 seasonal snowpack was at sub-zero temperature and free of ice layers. Snow and firn density were measured at 10-cm intervals in the firn pits, using a

100-cm^3 box cutter. The seasonal snow had an average density of 290 kg m^{-3}. The underlying summer 2015 melt surface took the form of an ice layer (i.e., a refrozen crust), which was difficult to penetrate with an avalanche shovel. Below this, the firn was made up of a mixture of dense snow, ice lenses and ice layers. There were 32 discrete ice layers in the upper 5.3 m of snow and firn, with a total ice thickness of 1.08 m. This is equivalent to an average ice-layer thickness of 3.4 cm. About half of the ice layers (15) were less than 1-cm thick and three layers exceeded 10 cm in thickness, with the maximum being a 33-cm thick layer extending from 3.79 to 4.12 m depth. Several ice layers were horizontally continuous over the ~2 m width of the firn pits (cf. Figure 1c).

Table 1. Installation depths (d) and initial snow/firn temperature (T_{s0}), bulk dielectric permittivity (ε_{b0}), and density (ρ_0) at each measurement level for sites A and B.

	Site A (installed May 11, 2016) 66.47775°N, 46.28510°W				Site B (installed May 8, 2016) 66.47505°N, 46.29115°W			
Level	d (m)	T_{s0} (°C)	ε_{b0}	ρ_0 (kg m^{-3})	d (m)	T_{s0} (°C)	ε_{b0}	ρ_0 (kg m^{-3})
1	0.3	–7.3	2.37	380	0.1	–3.7	2.31	280
2	0.6	–10.1	1.88	380	0.2	–4.2	2.49	310
3	0.9	–12.7	2.21	230	0.4	–6.6	2.09	280
4	1.4	–14.5	2.32	510	0.6	–9.2	2.06	320
5	1.8	–15.1	2.37	410	0.9	–11.9	2.47	640
6	2.1	–15.6	2.44	460	1.2	–13.1	2.54	620
7	2.8	–15.7	2.14	360	1.4	–14.4	2.65	560
8	3.7	–15.8	2.67	520	1.6	–14.9	2.36	480

The north-facing vertical face of each firn pit was instrumented with 8 thermistors and 8 time-domain reflectometry (TDR) probes to monitor snow water content (Table 1, Figure 1c). Sensors were inserted horizontally, with the thermistors and TDR probes extending 10 cm and 30 cm into the wall of the firn pit, respectively. Sensor spacing was irregular in order to concentrate observations near the surface as well as immediately above and below thick ice layers, to test whether these acted as impermeable barriers to water flow (Table 1). The firn pits were filled in with snow after sensor installation. The thermistors and TDR probes were wired to Campbell Scientific CR1000 dataloggers and values were recorded each 30 minutes from May 11 to September 30, 2016, capturing the subsurface hydrological and thermal evolution over the complete melt season.

2.2.2 Firn Cores

Firn cores reaching depths of 5 to 21 m were drilled with a Kovacs ice coring system in 2016 and 2017, including cores adjacent to each firn pit. The cores were analyzed at 5-cm vertical resolution for density and stable isotopes ($\delta^{18}O$, δD). Visual stratigraphies were carried out at 1-mm vertical resolution. The ice-layer stratigraphy in the firn cores supports the interpretation of the TDR data and also informs the total ice content in the firn, a measure of average melt/refreezing rates at the site.

2.2.3 TDR Data Analysis

Snow is made up of a mixture of ice, air, and liquid water, with differing dielectric properties for each constituent. We adopt fixed values for the relative dielectric permittivity of air, ice, and water: $\varepsilon_a = 1$, $\varepsilon_i = 3.2$, and $\varepsilon_w = 80$, respectively (Evans, 1965; Lundberg, 1997). Because of these differences, the dielectric permittivity of snow increases strongly with liquid water content, making the bulk value, ε_b, a sensitive indicator of snow moisture. For porosity θ and volumetric liquid water fraction θ_w, the bulk density of snow or firn is

$$\rho_b = \rho_i\,(1-\theta) + \rho_a(\theta - \theta_w) + \rho_w\theta_w\,, \qquad (1)$$

Where ρ_i is the density of ice crystals in the snow matrix (917 kg m^{-3}) and ρ_a and ρ_w are the densities of air and water (1.1 kg m^{-3} and 1000 kg m^{-3}, respectively). The dry density, ρ_d, is calculated from Eq. (1) when $\theta_w = 0$: $\rho_d \approx \rho_i\,(1-\theta)$ for dry snow/firn at temperatures below 0°C. This was the case on installation of our sensors, when we measured the initial snow and firn densities (Table 1). Snow density and water content both influence dielectric permittivity because solid and liquid water molecules are polarized in the presence of an electric field; a greater mass of these molecules increases polarization and relative permittivity (Stein et al., 1997; Schneebeli et al., 1997).

Measured dielectric permittivity needs to be converted to water content based on a dielectric mixing model. Empirical equations that relate TDR-derived dielectric permittivity to liquid water content have been developed for soils (e.g., Topp et al., 1980; Ledieu et al., 1986), but these are

not appropriate for snow or firn. Tiuri et al. (1984) and Denoth (1994) introduce empirical equations relating the bulk dielectric permittivity to snow density and water content. Stein et al. (1997), Schneebeli et al. (1997), Lundberg (1997), and Techel and Pielmeier (2011) discuss the specific application of TDR methods to snow, including empirical equations to separate the effects of snow density and liquid water content on the bulk dielectric permittivity.

Following work in soil water studies (Birchak et al., 1974; Roth et al., 1990), three-component mixing models have also been applied to analyses of bulk dielectric permittivity in snow,

$$\varepsilon_b = \varepsilon_i^{\beta}\,\theta_i + \varepsilon_w^{\beta}\theta_w + \varepsilon_a^{\beta}\theta\,. \tag{2}$$

Exponent β is equal to 0.5 for the Birchak et al. (1974) model, based on the relation between bulk dielectric permittivity and the volume-averaged wave velocity in a dielectric medium. Several recent snow radar studies also apply an exponent of 0.5 in dielectric mixing models (e.g., Schmid et al., 2014; Heilig et al., 2015, 2018). This choice of exponent was found to work well for TDR monitoring of meltwater content in supraglacial snow (Samimi and Marshall, 2017), giving:

$$\theta_w = \frac{\varepsilon_b^{1/2} - \varepsilon_i^{1/2}\,(1-\theta) - \varepsilon_a^{1/2}\theta}{\varepsilon_w^{1/2} - \varepsilon_a^{1/2}}\,. \tag{3}$$

The porosity θ can be calculated from Eq. (1) with dry density measurements (i.e., prior to the onset of the melt season), $\theta \approx 1 - \rho_d/\rho_i$. To update θ through the summer melt season, we include a model of snow and firn densification following Vionnet et al. (2012),

$$\frac{d\rho_d}{dt} = \frac{\rho_d \sigma}{\eta}\,, \tag{4}$$

for overburden pressure σ and snow/firn viscosity η. Vionnet et al. (2012) developed this parameterization of viscous deformation for the seasonal snowpack, but it has been applied to firn densification in several studies (e.g., Gascon et al., 2016; Verjans et al., 2019). The formulation includes a parameterization of the effects of temperature and liquid water content on

snow viscosity. This model for densification applies to the 'background' firn density (i.e., the firn matrix), and liquid water and refrozen ice content act in addition to this to increase bulk density, following Eq. (1).

2.3 Meteorological Data

2.3.1 Automatic Weather Station Data, 2016

An automatic weather station (AWS) configured for surface energy balance monitoring was installed adjacent to firn pit A in April, 2016 (Figure 2b). The AWS measured air temperature, humidity, incoming and outgoing longwave and shortwave radiation, wind speed and direction, air pressure, and snow surface height every 10 seconds, with 30-minute averages saved to the datalogger. Snow surface height was measured by an ultrasonic depth gauge (UDG) mounted on an independent stake that was drilled 2 m into the firn. Separate meteorological sensors were installed at Site B to measure air temperature, humidity, and snow surface height (Figure 2c). All sensors were left in place for one year, from April 2016 to April 2017.

The UDGs track both fresh snow accumulation events and surface drawdown. This provides information on the evolving burial depth for the TDR probes and thermistors and the potential melt-out of the sensors. Surface height increases due to snowfall events or windblow snow accumulation are also recorded by these sensors. Surface drawdown can occur through wind scour, sublimation, melting, and snow/firn densification, so interpretation is required to infer surface melt from the UDG records. We combine different lines of evidence to infer summer melt totals (in m w.e.) from these records. Initial measurements of snow density provide data for the snow-water equivalent of the snowpack and the density stratigraphy. We use the densification model (Eq. 4) to estimate vertical motion due to settling of the initial snow and firn stratigraphy and assume that the remaining surface drawdown signal is due to melting. Where snow accumulation is recorded by the UDGs, we assume that this represents fresh snowfall with an initial snow density of 120 kg m^{-3}, after Heilig et al. (2018). As a separate constraint, thermistors and TDR sensors that melt out have distinctive signals (e.g., daytime warming well above 0°C, which cannot occur in snow). This provides an independent estimate of the amount of ablation that occurred at a site, based on the snow-water equivalent that was removed above

any exposed sensors. We assume that any such ablation occurred due to melt. This can be cross-checked against the modelled melt from the surface energy balance, which provides an additional independent estimate of the melt.

Automatic weather station data are used as input to a surface energy balance model to estimate surface melt rates (Ebrahimi and Marshall, 2016) and inform the interpretation of the thermistor and TDR data. We also use the 30-minute AWS data to drive a model of firn evolution through the 2016 melt season. The surface energy balance and firn model are described in section 2.4. Thermistor and TDR data are used to constrain and tune the firn model, and we then apply the calibrated model to analyses of multi-decadal firn evolution at DYE-2, using meteorological forcing from GC-Net AWS (Steffen and Box, 2001) and ERA5 climate reanalyses (Hersbach et al., 2020).

2.3.2 GC-Net Weather Station Data, 1997-2018

For applications with more remote meteorological forcing (i.e., nearby weather stations; output from climate reanalyses or climate models) we use a slightly different configuration of the surface energy balance model. Specifically, outgoing shortwave and longwave radiation are calculated internally in the surface energy balance and firn model, based on the modelled surface albedo and the surface-layer temperature. Required input fields to drive the model include air temperature, relative humidity, wind speed, air pressure, and incoming shortwave and longwave radiation. With the exception of incoming longwave radiation, these fields are available from the GC-Net DYE-2 AWS data from 1997 to 2018. These data contain numerous gaps (see Vandecrux et al., 2018); the data were quality-controlled and gap-filled to provide mean daily values of all missing or compromised meteorological variables. Gap-filling was based on random sampling of the statistical distribution of all available data for a given day. For incoming longwave radiation, we use hourly ERA5 reanalysis data from the nearest 0.25° grid cell to DYE-2, at 66.5°N and 46.25°W. ERA5 incoming longwave radiation is biased-adjusted using daily mean bias corrections, based on comparison with our AWS data for the period April to October, 2016. The average bias adjustments for April and October are used for the months of November to March. Precipitation data (monthly snow accumulation) are also taken from ERA5 for the period 1997 to 2018.

The energy balance and firn models are run on 30-minute or hourly time steps. Where only daily mean data are available (i.e., for the gap-filled data), we use a parameterization of the diurnal cycles of temperature and incoming shortwave radiation to construct 30-minutes values from mean daily fields (Ebrahimi and Marshall, 2016). This parameterization requires minimum, maximum, and mean daily temperature and the mean and maximum daily incoming shortwave radiation.

2.3.3 ERA5 Climate Reanalyses, 1950-2020

Hourly ERA5 climate reanalyses are available at a resolution of 0.25° for the period 1950-2020 (Hersbach et al., 2020). We compiled this into daily mean data for the grid cell at 66.5°N and 46.25°W which contains DYE-2. Incoming longwave radiation was bias-adjusted as noted above. For the remaining ERA5 data, daily bias adjustments are applied based on mean deviations in the ERA5 data from the gap-filled GC-Net data over the common period 1997-2018. The firn model is forced by the mean daily bias-adjusted ERA5 meteorological fields, with parameterizations of the diurnal temperature and incoming shortwave radiation cycles and surface albedo and outgoing longwave radiation modelled internally, as noted above.

Daily mean meteorological forcing is used for the ERA5 simulations for pragmatic reasons. It is simpler to bias-adjust and gap-fill than 30-minute or hourly data and it is also readily available from a wide range of climate reanalyses and future climate projections. As this is of interest to follow-up work with ice-sheet scale firn modelling, we focus on tuning and calibration of the surface energy balance and firn model to these inputs. Ebrahimi and Marshall (2016) demonstrate that modelled surface energy balance and melt using daily mean forcing is in good accord with hourly forcing, as long as diurnal cycles of air temperature and incoming shortwave radiation are accounted for.

2.4 Surface Energy Balance and Firn Model

2.4.1 Model Physics and Parameterizations

Surface energy balance and melt rates are calculated following the model of Ebrahimi and Marshall (2016), including a subsurface model for heat conduction in the upper 20 m of firn and snow. The model has 43 layers, with resolution concentrated near the surface; layers are 0.1-m thick from the surface to a depth of 0.6 m, 0.2-m thick from 0.6 to 2 m, 0.4-m thick from 2 to 10 m, and 1-m thick from 10 to 20 m. Net energy, Q_N, is calculated at 30-minute intervals as the sum of the energy fluxes towards the surface layer,

$$Q_N = Q_S^{\downarrow} - Q_S^{\uparrow} + Q_L^{\downarrow} - Q_L^{\uparrow} + Q_H + Q_E + Q_C, \quad (5)$$

where the terms on the right represent (in order) the incoming and outgoing shortwave radiation, incoming and outgoing longwave radiation, and the sensible, latent, and conductive heat fluxes. The model requires inputs from either AWS data or climate reanalyses/models for the incoming shortwave and longwave radiation, wind speed, air temperature, humidity, and air pressure. Sensible and latent heat flux are calculated from these meteorological fields and conductive heat fluxes are calculated within the subsurface model, based on the temperature gradient in the upper three layers. Reflected shortwave radiation $Q_S^{\uparrow} = Q_S^{\downarrow} (1 - \alpha_s)$, for surface albedo α_s, and outgoing longwave radiation $Q_L^{\uparrow}$ follows Stefan-Boltzmann's equation, $Q_L^{\uparrow} = E_s \sigma T_s^4$, for surface emissivity E_s = 0.98, Stefan-Boltzmann's constant σ, and absolute temperature of the surface layer, T_s. Albedo and surface temperature are calculated internally (Ebrahimi and Marshall, 2016), or AWS data can be used directly for these where data are available (i.e., summer 2016).

When the surface layer is at 0°C and $Q_N > 0$, net energy goes to melting, following

$$\dot{m} = Q_N/(\rho_w L_f), \quad (6)$$

where $\dot{m}$ is the melt rate (m s^{-1}), and L_f is the latent heat of fusion. If net energy is negative and the surface layer is 0°C, any liquid water that is present will refreeze, releasing latent heat, and the surface layer will cool once all liquid water is refrozen. When surface layer temperatures are below the melting point, and surplus or deficit of energy drives warming or cooling, based on the energy balance solution within a one-dimensional model of subsurface temperature evolution:

$$\rho_b c_b \frac{\partial T}{\partial t} = \frac{\partial}{\partial z}\left(-k_t \frac{\partial T}{\partial z}\right) + \varphi_t + \rho_w c_w q_w \frac{\partial T_w}{\partial z}. \quad (7)$$

The right-hand terms represent heat conduction, latent heat release from meltwater refreezing, and heat transport from advection of meltwater or rainwater, respectively. Here ρ_b, c_b and k_t are the bulk density, specific heat capacity, and thermal conductivity of the snow or firn, ρ_w and c_w are the density and specific heat capacity of water, and q_w is the vertical rate of water percolation, with units m s^{-1}. We calculate the thermal conductivity of the snow and firn after Calonne et al. (2019). The specific heat capacity of ice is taken from Cuffey and Paterson (2010), $c_i = 152.2 + 7.122\ T_k$, for absolute temperature T_k. Bulk heat capacity is then calculated from $c_b = [\rho_i\ (1–\theta)\ c_i + \rho_w \theta_w c_w]/\rho_b$.

The refreezing term in (5) has units W m^{-3} and is calculated from

$$\varphi_t = \frac{\rho_w L_f \dot{r}}{\Delta z}, \quad (8)$$

where $\dot{r}$ is the refreezing rate (m s^{-1}) and this heat is spread across the layer thickness, Δz.

The subsurface temperature model is coupled with a simple treatment of meltwater percolation. For a snow or firn layer with thickness Δz and the volume fraction of liquid water θ_w, the amount of water in the layer (m) is equal to $\theta_w \cdot \Delta z$. The local water balance in each subsurface layer is then:

$$\frac{d\theta_w}{dt} = -\nabla \cdot q_w - \frac{\dot{r}}{\Delta z}. \quad (9)$$

Any water that refreezes is assumed to be distributed over the layer Δz. We assume that all meltwater flow is vertical (gravitational drainage with no horizontal advection), such that the flux divergence in Eq. (9) is calculated from the vertical derivative and

$$\frac{d\theta_w}{dt} = -\frac{dq_w}{dz} - \frac{\dot{r}}{\Delta z} = \frac{1}{\Delta z}\left(q_{wu} - q_{wl} - \dot{r}\right), \quad (10)$$

where q_{wu} and q_{wl} refer to the meltwater flux into (upper boundary) and out of (lower boundary) the layer. At the upper boundary, this is equal to the melt rate. Refreezing in Eq. (10) is calculated within the subsurface thermal model, accompanied by latent heat release as calculated from Eq. (8).

Once a layer is temperate, liquid water can be retained within the pore space or it can percolate deeper into the snow or firn. Each layer can retain a certain amount of water within its pores due to capillary forces, the irreducible water content. We follow the formulation from Coléou and Lesaffre (1998), where the irreducible water is expressed as a fraction of total mass:

$$\theta_{mi} = 0.017 + 0.057 \, \frac{\theta}{1-\theta} \, . \tag{11}$$

The porosity θ is calculated from the dry snow and ice densities in Eq. (1) , based on initial field measurements and the snow compaction model for melt-season densification (Eq. 4). For bulk snow/firn density ρ_b and water density ρ_w, the volume and mass fractions of liquid water are related through:

$$\theta_{wi} = \theta_{mi} \frac{\rho_b}{\rho_w} \, . \tag{12}$$

Note that we define the volumetric water content θ_w and the irreducible water θ_{wi} based on the total snow or firn volume, in contrast to some earlier work (e.g., Colbeck, 1974) that refers to the volume fraction within the pore space.

Any water in excess of the irreducible water content is allowed to move downward. We calculate the water flux from a transport equation of the form,

$$q_w = -k_h \nabla \phi, \tag{13}$$

for effective hydraulic conductivity k_h and hydraulic potential ϕ (in m). Our reference value for the hydraulic conductivity is $k_{h0} = 10^{-5}$ m s^{-1} (Fountain and Walder, 1998), but we experiment with values of 10^{-3} to 10^{-7} m s^{-1} in the model and examine the TDR observations of meltwater infiltration to constrain this. Eq. (13) in equivalent to Darcy's law, which applies to saturated flow and can be applicable in saturated firn, where water pressure gradients contribute to the flux (e.g., Christianson et al., 2015). For unsaturated, gravitational percolation, the hydraulic gradient is equal to the vertical distance, $\Delta z/\Delta z = 1$, and the vertical percolation velocity $q_w = k_h$. This is an expression of the wetting front propagation speed of free water in the pore space (i.e., that which is not retained by capillary tension) and is not equivalent to the saturated hydraulic conductivity. We treat k_h as a constant where ice layers are less than 0.1 m thick, based on evidence of meltwater penetration through layers up to 0.12 m thick at DYE-2 (Samimi et al., 2020). We assume that ice layers more than 0.5 m thick act as impermeable 'ice slabs' (MacFerrin et al., 2019). For ice layers with thickness t_i between 0.1 m and 0.5 m, we prescribe $k_h = k_{h0} \cdot 10^{-\gamma\,(ti\,-\,0.1)}$. For $k_{h0} = 10^{-5}$ m s^{-1} and $\gamma = 5$, our reference values, k_h decreases from 10^{-5} to 10^{-7} m s^{-1} as ice-layer thickness increases from 0.1 to 0.5 m.

We solve the subsurface temperature and hydrological evolution in Eqs. (7) and (10) using 30-minute time steps through the summer melt season, permitting a direct comparison with the TDR probe and thermistor data at the different measurement depths. The simulations for summer 2016 use the observed spring snowpack as an initial condition and model densification following Eq. (4), along with the effects of modelled ice layers that form from meltwater refreezing. For the multi-year simulations forced by GC-Net and ERA5 meteorological fields, monthly snow accumulation at DYE-2 is taken from the ERA5 precipitation. Layers in the firn model are added or removed as snow accumulates and ablates, effectively advecting accumulated snow and ice-layer stratigraphy through the model grid.

2.4.2 Firn Model Initialization

The subsurface model requires initial conditions over the 20-m depth of the firn column. For the ERA5 simulations, we run the model through a 40-year spin-up over the period 1950 to 1990, then restart the simulation at 1950 with the spun-up temperature, density, and ice-layer

543 stratigraphy as initial conditions. A 40-year spin-up is adopted because this is the approximate
544 number of years represented in the upper 20 m of firn (Mosley-Thompson et al., 2001).
545
546 For numerical experiments forced by the GC-Net AWS record, 1997 to 2018, we take the spun-
547 up firn conditions from the ERA5 simulations from 1950 to December 31, 1996, then apply the
548 AWS forcing from the gap-filled GC-Net station record as of January 1, 1997. For simulations of
549 just the 2016 melt season to compare with the thermistor and TDR records, the model is
550 initialized with the observed snow/firn thermistor temperatures, densities, and ice layers in the
551 upper 3.5 m of the snow and firn (April 2016). Below this, densities and ice-layer stratigraphy
552 are based on measurements from the 21-m firn core. Initial temperatures below 3.5 m are taken
553 from the GC-Net simulations for May 1, 2016.
554
555 *2.4.3 Model Sensitivity Experiments and Evaluation*
556
557 Model results are compared with the 2016 observational dataset to examine one of the most
558 uncertain process parameterizations in the firn model, the treatment of capillary water retention
559 (van As et al., 2016; Samimi et al., 2020). Most previous firn modelling studies adopt either
560 Coléou and Lesaffre (1998) or use a fixed value $\theta_{wi} = 0.02$ (e.g., Reijmer et al., 2012; Verjans et
561 al., 2019; Vandecrux et al., 2020b). Our reference model uses Eq. (11) from Coléou and Lesaffre
562 (1998), but we also carry out experiments with fixed values of the irreducible water content from
563 0.002 to 0.04 and with a simple scaling of Eq. (11), from 50% to 150%. The latter approach
564 assumes that capillary water retention varies with depth (porosity), in proportion with the
565 empirical relation of Coléou and Lesaffre (1998).
566
567 Model results are evaluated against three different observations from the summer 2016 field
568 studies: firn temperatures, T_f, maximum meltwater infiltration depth, z_w, and total summer melt,
569 m. Firn temperatures are compared directly at all eight levels, and we evaluate model
570 performance based on mean absolute error (MAE), mean error, and mean rms error of modelled
571 vs. observed temperatures. We also construct a composite model performance index, I, to
572 evaluate the model results based on all three observed fields of interest, derived from the
573 standardized model deviations (model minus observation) of firn temperature, ΔT_f, meltwater

infiltration depth, Δz_w, and summer melt, Δm:

$$I = 1 - \frac{1}{3}\sqrt{\left(\frac{\Delta T_f}{\sigma_T}\right)^2 + \left(\frac{\Delta z_w}{z_w}\right)^2 + \left(\frac{\Delta m}{m}\right)^2}. \quad (14)$$

Mean absolute error is used as a measure of ΔT_f and σ_T is the mean standard deviation of observed firn temperature at all levels. An index of $I = 1$ indicates a perfect match with observations. $I \in (0,1)$ for all model experiments that we carried out, though this index can be negative if model deviations are large. Variables in (14) can be weighted according to the relative importance of each field, but we assign them equal weights in our evaluation.

3 Results

3.1 AWS Observations and Surface Energy Balance

Figure 2 plots meteorological and surface energy balance conditions through summer 2016, spanning the melt season at DYE-2. Snow surface temperature in Figure 2a is calculated from the measured outgoing longwave radiation, $T_s = (Q_L{}^{\uparrow}/\sigma E_s)^{1/4}$. There was a minor surface thaw while we were in the field in early May, with temperatures reaching 0°C, but the subsurface remained below the melting point through this period and there was no evidence of subsurface meltwater. A thin (~1 mm) ice layer was observed at the snow surface. Two colder weeks followed, during which time the seasonal snow cooled to below −13°C. The snowpack remained dry throughout the month of May, while we were at the site. The melt season began the first week of June and ran through to late August (Figure 2a). Diurnal cycles of air and snow-surface temperature indicate a daily freeze-thaw cycle through most of the melt season, with surface refreezing at low solar radiation angles ('overnight'). Air and snow-surface temperatures reach 0°C for a few hours on most days through the summer (JJA) melt period, with two occasions when melt conditions persisted through the night (July 18-19 and August 9-11).

Net longwave radiation was consistently negative save for two overcast periods on the dates noted above, when snow and air temperatures remained near 0°C. This drove high values of incoming longwave radiation and net energy (Figure 2c), giving the highest melt rates of the

603 summer (Figure 2d). Net radiation was positive over the summer (JJA), averaging 14 W m^{-2},
604 while sensible, latent, and conductive heat fluxes averaged +3, −11, and +1 W m^{-2}, respectively
605 (Table 2). Net energy averaged 5 W m^{-2} for the summer and was maximum in July, 10 W m^{-2}. It
606 declined to 3 W m^{-2} in August, due to the reduced shortwave radiation and atmospheric cooling,
607 but early August meltwater production was nonetheless significant, exceeding that of June and
608 representing about 32% of the summer total. Conductive heat flux to the surface was more
609 important in August and September, averaging ~3 W m^{-2}.
610
611 UDG snow surface height measurements at the two firn pits indicate a total summer melting of
612 about 0.5 m of snow or 0.18 ± 0.04 m w.e. (Figure 2b). Summer snow events partially offset the
613 melting, resulting in ~0.25 m of ablation relative to the April snow surface (Figure 2b). The
614 upper two sensors at site A, at depths of 0.1 and 0.2 m, melted out on July 25 and July 30,
615 respectively. Data from these sensors is omitted from the analysis after these dates. Sensors at
616 and below 0.3 m depth remained below the surface through the full melt season. The surface
617 energy balance model gives an estimated total melt of 0.40 m w.e. from May through September
618 (Figure 2d). About half of the melt occurred in July, when net radiation was the strongest. The
619 total includes melting of refrozen near-surface ice lenses and pore water, which we call
620 'recycled' melt. Accounting for this, ablation or 'net melt' is much less than the total melt. Net
621 summer melt equals 0.16 m w.e. with the reference model, although this result depends on the
622 parameter settings for capillary water retention (see section 3.4).
623
624

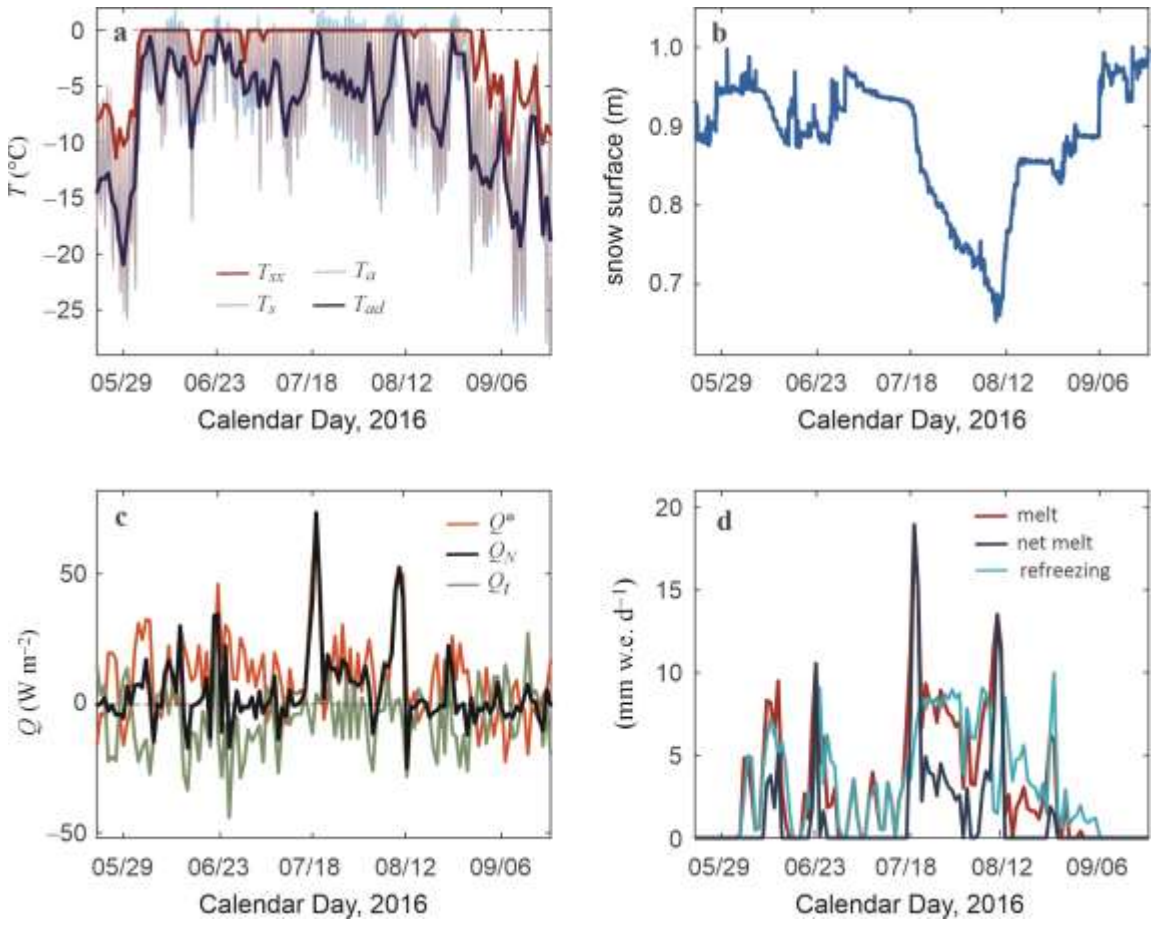

Figure 2. Meteorological data and modelled surface energy balance at DYE-2 over the summer melt season, May 24 through September 18, 2016. (a) Average 30-minute values of air and snow-surface temperature, T_a and T_s, daily average air temperature, T_{ad}, and daily maximum snow-surface temperature, T_{sx}. (b) Ultrasonic depth gauge (UDG) record of snow-surface height. (c) Mean daily net radiation, Q^*, turbulent flues, Q_t (sensible plus latent heat fluxes), and net energy, Q_N. (d) Daily total melt, net melt (ablation), and refreezing. Net melt refers to the surface melt that infiltrates below the surface layer and total melt includes refrozen near-surface meltwater (i.e., 'recycled' mass).

Table 2. Mean monthly and summer (JJA) surface energy fluxes and melt totals, summer 2016. All energy fluxes (Q) have units W m^{-2}, α is the surface albedo, T_a is the mean air temperature (°C), *PDD* denotes positive degree days (°C d), and *melt* reports monthly and summer totals (m w.e).

Period	$Q_S^{\downarrow}$	$Q_S^{\uparrow}$	α	$Q_L^{\downarrow}$	$Q_L^{\uparrow}$	Q_H	Q_E	Q_C	Q_N	T_a	*PDD*	*melt*
May	303	252	0.83	211	266	9	–9	0.1	0	–11.6	0.6	0.02
June	330	272	0.82	255	298	2	–14	–0.3	4	–4.0	1.8	0.09
July	341	256	0.75	227	296	6	–11	0.2	9	–4.1	2.7	0.17
Aug	252	189	0.75	237	289	2	–9	1.4	5	–5.7	2.4	0.12
Sept	143	117	0.82	222	250	2	–6	1.4	–1	–14.5	0.0	0.00
JJA	308	239	0.78	239	295	4	–12	0.4	6	–4.6	6.9	0.38

All of the meltwater refroze in the snow and firn. Many days have strong diurnal melt-freeze cycles, with identical daily melt and refreezing totals (Figure 2d). At other times, refreezing lags melting by a few days, reflecting meltwater that infiltrates isothermal snow or firn and remains as liquid water for a short while. Table 3 lists the monthly and summer partitioning between melt, ablation, refreezing, and the different energy fluxes within the subsurface model. Of 234 MJ m^{-2} in total positive net energy over the summer, 100 MJ m^{-2} (43%) went to warming the near-surface snowpack and 134 MJ m^{-2} (57%) was directed to melting. The latent heat released in the near-surface snow and firn during refreezing was identical to the melt energy, 134 MJ m^{-2}, as 100% of meltwater refroze.

Table 3. Monthly, summer, and melt-season (MJJAS) mass and energy fluxes for the reference model parameter settings. m, m_s and r refer to the total monthly or summer melt, the net melt (surface ablation associated with melting, including the effects of 'recycled' meltwater), and refreezing. E_{warm} is the total surface energy used to warm the surface layer of the snow (when $T_s < 0$ and $Q_N > 0$), E_{melt} is the energy used for melting (when $T_s = 0$ and $Q_N > 0$), E_{adv} is the sensible heat advection associated with meltwater infiltration, and E_{ref} is the latent heat energy released by meltwater refreezing.

	Mass balance (m w.e.)			*Energy fluxes* (MJ m^{-2})			
Period	m	m_s	r	E_{warm}	E_{melt}	E_{adv}	E_{ref}
May	0.02	0.01	0.02	30	7	0.0	7
June	0.09	0.03	0.09	18	31	0.1	31
July	0.17	0.08	0.14	23	55	0.3	47
Aug	0.12	0.05	0.14	23	41	0.2	47
Sept	0.00	0.00	0.01	24	2	0.1	7
JJA	0.38	0.15	0.37	64	127	0.6	125
MJJAS	0.40	0.16	0.40	117	135	0.6	135

3.2 TDR and Thermistor Observations

Figure 3 plots measured subsurface temperatures and liquid water content in the two firn pits through summer 2016. The melt-season progression was similar at the two sites, with nearly identical timing and depth for the meltwater infiltration and subsurface warming events. There were three main periods of melting in summer 2016, indicated by the grey shading. The first major melt event was in the second week of June, with meltwater infiltration to a depth of 0.2 m, as recorded by the two upper two sensors at site B (Figures 3e,f). The snow at 0.4 m depth remained below 0°C and dry during this initial event. This initial meltwater infiltration episode was also undetected by the upper sensors at site A, at 0.3 m (Figure 3c), so appears to have been

689 confined to the upper 0.2 m of the snowpack. Sensors at 0.3 m and 0.4 m depth warmed to near
690 0°C during this event, but an atmospheric cooling cycle followed and the entire snowpack
691 refroze and cooled.
692

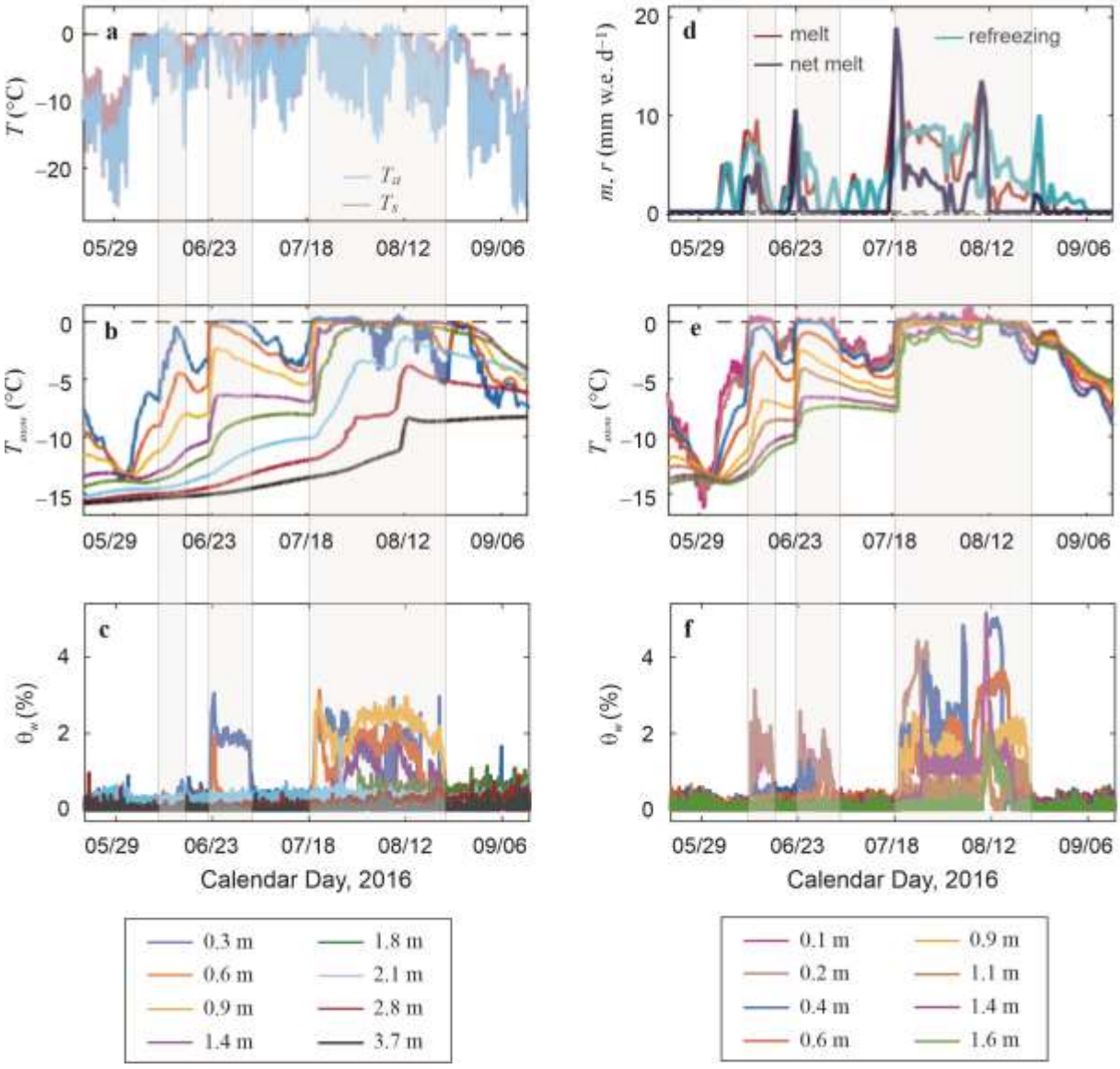

693
694
695 **Figure 3.** Observed (a) air and snow surface temperatures, (b,e) snow temperatures, and (c,f) liquid water content,
696 along with (d) modelled melt and refreezing, summer 2016. (b,c) are for firn pit A and (e,f) are for firn pit B. Shaded
697 areas indicate periods of meltwater infiltration indicated by the subsurface temperature and liquid water content
698 measured at firn pit B.
699

700 Melting resumed on June 22, accompanied by an abrupt warming of up to 5°C in the upper ~1.4
701 m of snow and firn and wetting to ~0.5 m depth at both sites (Figures 3c-f). The warming was

recorded over less than 24 hours, evidence of latent heat release from refreezing meltwater, followed by slower conductive warming at firn depths below ~2 m. A detailed analysis of the meltwater infiltration event on June 22-23 provides a quantitative illustration of the coupled thermal and hydrological evolution during this abrupt warming and meltwater infiltration event (Figures 4a and 4b). Average air temperature was −1.1°C over this 48-hour period, with a maximum temperature of +1.2°C. Total modelled melt on these two days equals 13.6 mm w.e., with the onset of melt at 11:00 on June 22. By that evening, wet, temperate conditions developed to 0.6 m depth at site A and 0.4 m depth at site B. Temperatures at 11:00 on June 22 at 0.1, 0.2, 0.4, and 0.6-m depth were −2.6, −2.7, −3.5, and −5.2°C, respectively. Snow rapidly warmed at these four depths, reaching 0°C between 18:00 and 19:00 in the upper 0.6 m at site A and between 18:00 and 20:00 in the upper 0.2 m at site B. Sensors at 0.4 m depth at site B first recorded temperate, wet conditions at 08:00 on Jun 23. All sensors in the upper 0.5 m of snow then maintained temperate conditions for the next several days at the two sites.

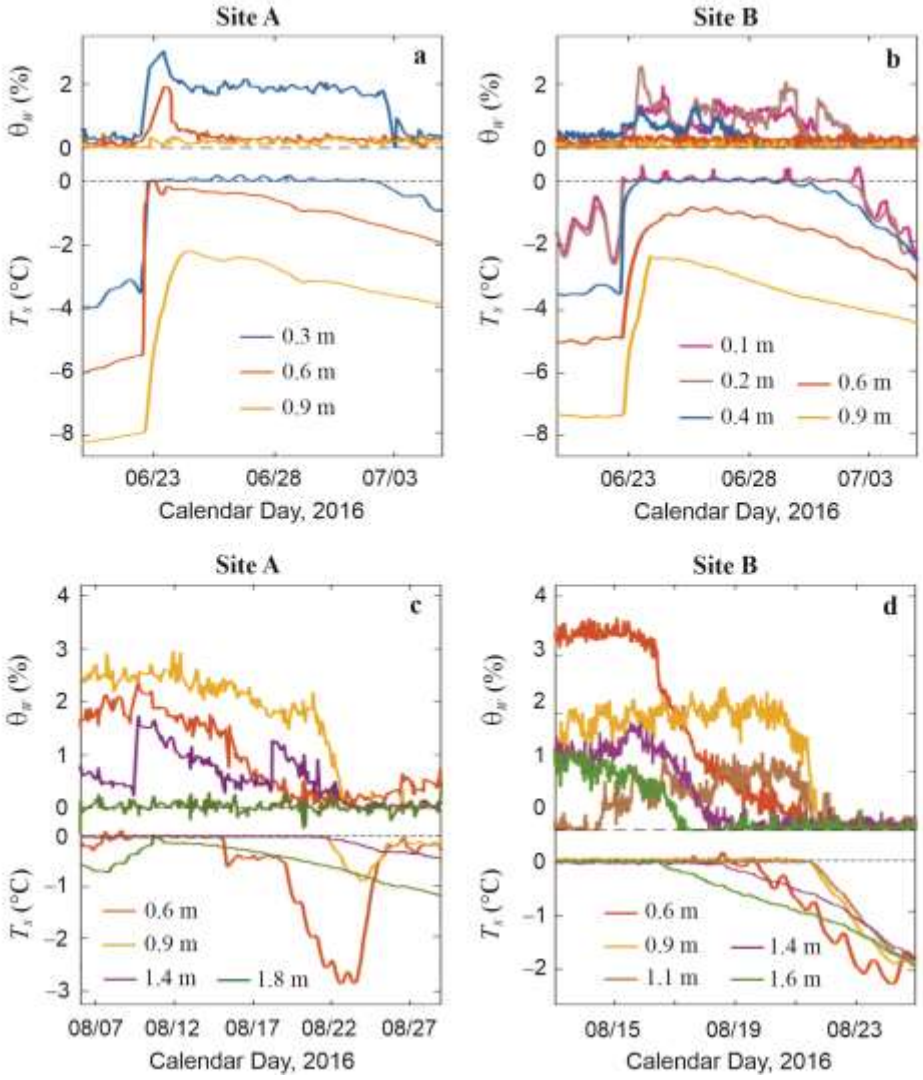

Figure 4. Observed snow/firn liquid water content (top of each panel) and temperature (bottom of each panel) for select periods of interest in the summer 2016 melt season. (a,b) Melt onset at Sites A and B for the period June 21 to July 4, for all sensors at depths less than 1 m. (c) Records from 0.6- to 1.4-m depth at Site A from August 6-28, indicating the arrival of the thaw front (0°C isotherm) at 1.8-m depth on August 11 and the subsequent refreezing and cooling as the melt season shut down. (d) Records from 0.6- to 1.6-m depth at Site B during the melt season shutdown, August 13 to 25.

Dielectric permittivity (liquid water content) increased from background values at the same time as snow became temperate at each site during this initial melt event, with a simultaneous arrival of the thaw and wetting fronts at each depth. This melt cycle ended on July 2 at each site, as atmospheric cooling caused meltwater refreezing followed by cooling of snow temperatures. The thermistor and TDR measurements were highly consistent through this melt event, with θ_w = 1-2% under melting conditions and $\theta_w \sim 0$ when temperatures were below 0°C.

Following a two-week cool hiatus with limited surface melting, the melt season resumed in earnest on July 18 (Figure 3). The snow and firn had returned to dry, sub-zero conditions, so the next melt episode was again attended by an abrupt warming event. Melt conditions persisted for about one month this time, with temperate conditions developing to 1.8 m depth by August 10. All of the sensors at site B registered liquid water and melting temperatures (Figure 4d). At site A, the upper three sensors were wet and temperature through most of this record, through to August 23, while the sensors at 1.8 m depth reached the melting point for only a short interval (four hours on August 10), with a small, simultaneous increase in dielectric permittivity. Sensors below 1.8 m depth at site A maintained sub-zero temperature with no evidence of meltwater. The thaw and wetting fronts therefore briefly reached a depth of 1.8 m. Volumetric water contents of 3 to 4% were common in the upper 0.6 m during the main melt July-August episode, with short-lived values of up to 5% during the early stages of the main meltwater infiltration events. Water content in wetted firn was typically 1 to 2% at depths greater than 0.6 m

Declining shortwave radiation and cooler air temperatures in the second week of August triggered the end of the melt season, although it took several days for the firn to refreeze and cool. Figures 4c and 4d plot the end of the melt season at mid-depths (0.6 to 1.8 m) at each of the sites. During the last stages of refreezing, an isothermal, wet layer of snow and firn from ~0.6 to ~1.1 m depth was sandwiched between colder snow above and below. Cooling fronts moved down through the snowpack from the surface and also upward from the cold, underlying firn. The step-wise drying and refreezing at different depths is particularly clear in pit B in Figure 4d, with the deeper firn being the first to refreeze (at 1.6 m and then 1.4 m), followed by refreezing at 0.6, 0.9, and 1.1 m. It took about one week for the upper 1.8 m of snow and firn to refreeze and start cooling below 0°C, with the firn at ~1 m being the last portion of the seasonal thaw layer to refreeze. Small melt events after ~August 21 (Figure 3) appear to have refrozen near the surface, with no indication of subsurface liquid meltwater at either site after this time.

3.3 Firn Modelling, 2016 Melt Season

Figure 5 plots the modelled subsurface temperature evolution in the upper 4 m of the snow and firn for the reference model parameter settings. Observed air and subsurface temperatures at Site A are also plotted in Figure 5, for comparison. Diurnal freeze-thaw cycles at the surface are well

represented in the model, and are generally restricted to the upper ~0.2 m of the snow. The abrupt subsurface warming events during the main pulses of melt are captured by the model (Figures 5b and 5c), and are part of a stepwise penetration of the thawing and wetting front through the summer melt season. The model also reproduces the isolated warm layer that was observed at ~0.6 to 1.2 m depth during the August freeze-up. However, temperate conditions reached a maximum depth of 1.2 m in the second week of August in the model, which is an underestimate relative to the observed thaw front penetration to 1.8 m.

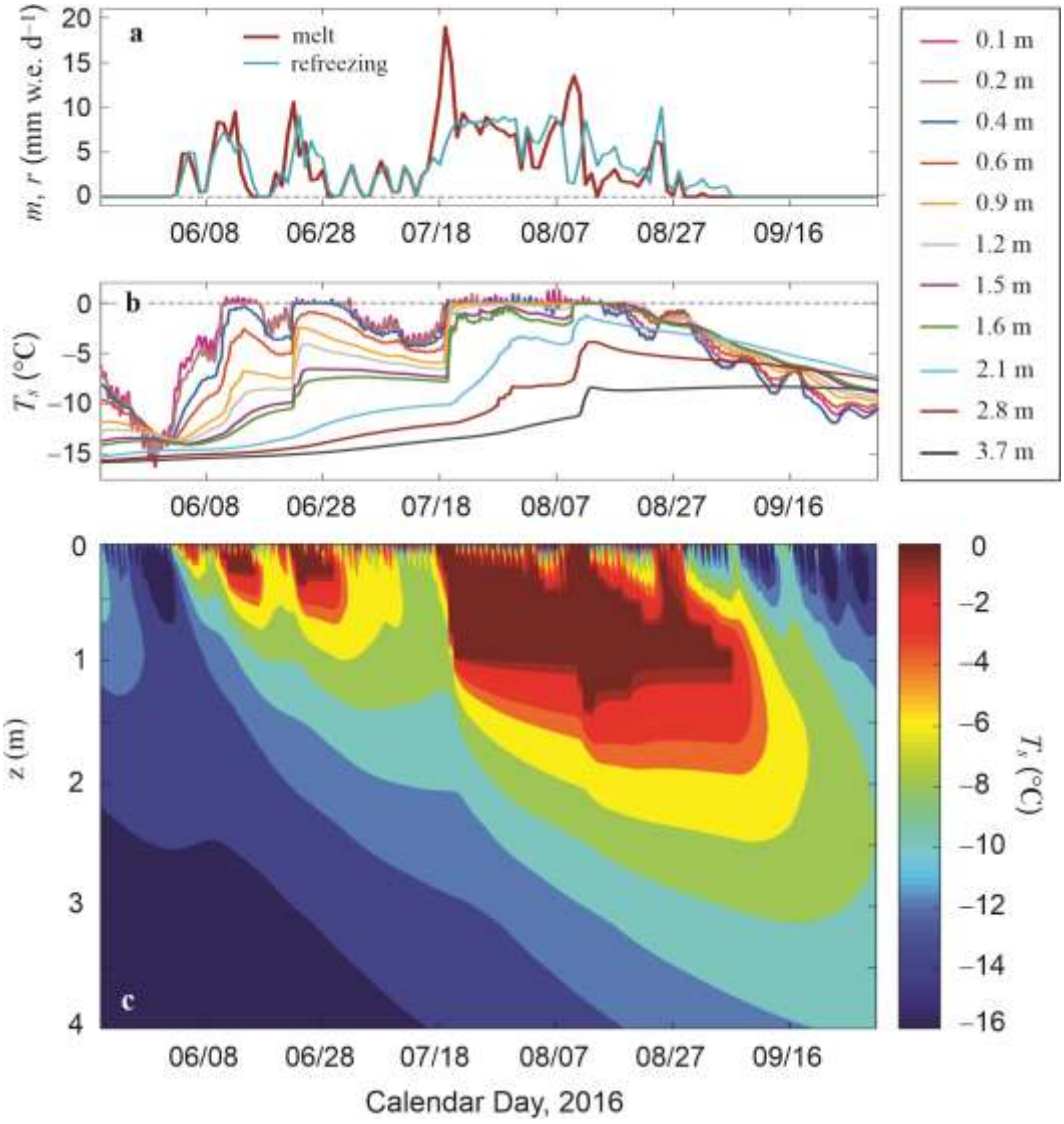

Figure 5. Results for the reference model parameter settings, with meltwater retention after Coléou and Lesaffre (1998). (a) modelled melt and refreezing, (b) observed subsurface temperatures at Site B, for comparison, and (c) modelled subsurface temperature evolution in the upper 4 m of snow and firn.

Modelled temperatures are highly correlated with the observations, with an average melt-season linear correlation coefficient of 0.96 over the eight observations depths from Site A (Table 4). The mean bias in the modelled temperature is –1.1°C, with a mean absolute error of 1.4°C. Modelled net summer melt equals 0.16 m w.e. with the reference parameter settings. This is within the uncertainties but about 10% less than the estimated summer melt based on the ultrasonic depth sensors, 0.18 ± 0.04 m w.e. Both subsurface temperatures and meltwater infiltration are underestimated compared with the observations. We do not simulate preferential flow paths that can lead to enhanced infiltration (e.g., Wever et al., 2014), so meltwater may be retained or refrozen too near the surface, contributing to the cold bias in the firn temperatures. Modelled meltwater infiltration is also highly sensitive to the parameterization of capillary water retention, as explored in the next section.

Table 4. Model comparison with observations for different treatments of irreducible water content for the 2016 melt season. The observed summer melt m = 0.18 m w.e. and thaw depth z_{thaw} = 1.8 m. ME, MAE, and RMSE are the mean, mean absolute, and mean rms errors in the modelled temperatures, averaged over the summer for all observation depths, r_T is the linear correlation coefficient between the observed and modelled temperatures, and I is the composite skill index for the model. Bolded values indicate the optimal model performance for a given measure.

θ_{wi} model	m (m w.e.)	z_{thaw} (m)	r_T	*ME* (°C)	*MAE* (°C)	*RMSE* (°C)	I
Reference	0.16	1.2	0.96	**–**1.07	1.44	2.01	0.84
CLp8	**0.19**	1.4	0.96	**–**0.82	1.27	1.78	0.88
CLp7	0.21	1.6	0.96	**–**0.67	1.16	1.63	**0.89**
CLp6	0.23	**1.8**	0.97	–0.38	0.95	1.32	**0.89**
CLp5	0.25	2.0	**0.98**	**–0.05**	**0.77**	**1.06**	0.85
0.04	0.16	1.0	0.96	**–**1.28	1.60	2.17	0.79
0.03	0.20	1.2	0.96	**–**1.00	1.51	1.91	0.85
0.02	0.25	**1.8**	0.97	–0.40	0.97	1.34	0.85
0.01	0.32	2.4	0.95	0.92	1.46	1.90	0.69

3.4 Sensitivity of the modelled meltwater infiltration to capillary water retention

Figure 6 plots modelled summer melt and the maximum depths of the thaw and wetting fronts as a function of θ_{wi}. Greater near-surface meltwater retention (higher θ_{wi}) limits meltwater infiltration and also reduces net melting, since a higher proportion of meltwater is recycled in near-surface freeze-thaw cycles. The blue shading in Figure 6 indicates the observed values and uncertainty range for meltwater infiltration depth and summer melt. The thaw front reached 1.8 m in our TDR data, but Heilig et al. (2018) estimate a maximum meltwater infiltration depth of

2.2 m, so we accommodate that possibility in the uncertainties. Averaged over the snow and firn column, the reference model parameterization from Coléou and Lesaffre (1998) gives a value θ_{wi} = 0.0273 (2.73%). Results are plotted against the mean value in Figure 6, but θ_{wi} varies with depth, following Eq. (11), with higher values near the surface. For a given mean value of θ_{wi}, melt totals with irreducible water content based on Eq. (11) are systematically lower than for uniform θ_{wi} (Figure 6), and are in better accord with the observed melt.

Table 4 summarizes model results for a selection of the experiments in Figure 6. No treatment of the capillary water retention simultaneously optimizes the fit to the different observations. For instance, a scaling factor of 0.5 applied to the parameterization of Coléou and Lesaffre (1998), which we denote CLp5, gives the best fit to the observed subsurface temperatures, but this comes at the expense of a large overestimation of the net melt (0.25 m w.e.) and meltwater infiltration depth (2.4 m). We evaluate the model based on the composite index *I*, which includes the agreement with observed firn temperatures, maximum summer meltwater infiltration depth, and net summer melt. The optimal value of capillary water retention is lower than that of our reference model, through a scaling factor of 0.7 for the parameterization of Coléou and Lesaffre (1998), which we denote CLp7. This gives the best combined fit to the three observational criteria, I = 0.89. We adopt this as the optimized model for decadal-scale simulations. The average irreducible water content with this setting is 0.019. For uniform values of the irreducible water content, the optimal results were for θ_{wi} = 0.025, but this setting gives both an over-estimate of melt and an underestimate of meltwater infiltration.

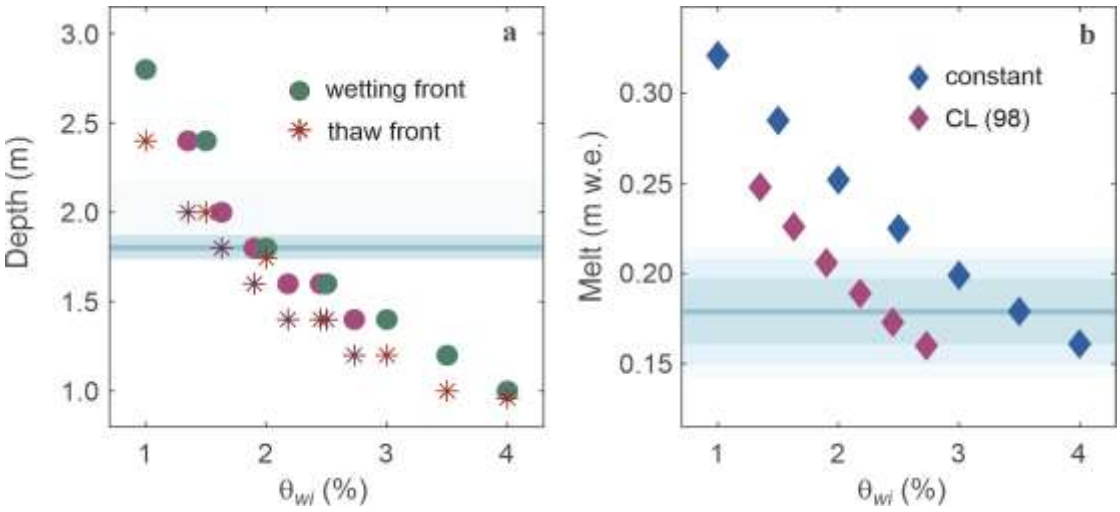

Figure 6. Sensitivity of modelled (a) maximum summer thaw and meltwater infiltration depth and (b) net surface melt to the parameterization of capillary water retention. The observed thaw front depth, 1.8 to 2.2 m, and net summer melt, 0.18 ± 0.04 mm w.e., are indicated with the blue lines, with shading indicating the estimated confidence range. Purple symbols are for the mean (depth-averaged) values of θ_{wi} from the Coléo and Lessafre (1998) parameterization and the green circles, red stars, and blue diamonds are for uniform values of irreducible water content.

Figure 7 plots modelled vs. observed mean daily subsurface temperatures at five different depths for the CLp7 model configuration. This has a higher correlation of temperatures, lower temperature error, and greater meltwater infiltration depth than the reference model (Table 4), in better accord with the observations, but net summer melt is 0.21 m w.e., about 0.03 m greater than observed. The model is slightly too cold below ~0.6 m depth; it is possible that the model thermal conductivity is too low, such that near-surface warming from latent heat release does not adequately conduct to depth. Consistent with this possibility, observed abrupt warming events from 2-4 m depth are more diffuse in the model (Figures 7c,d). These sudden warmings, with a magnitude of about 5°C, are well reproduced in the near-surface firn (Figures 7a,b).

3.5 Multi-Decadal Firn Evolution

Multi-year simulations with the CLp7 parameter settings provide insight into the interannual variability of meltwater infiltration depths and longer-term trends in firn temperature, density, and ice content at DYE-2. Over the period of available AWS data at the DYE-2 GC-Net station, 1997-2018, mean summer (JJA) temperature (± 1σ) was –5.4 ± 1.1°C, with no statistically significant trend (Figure 8a). Summer temperatures from the ERA5 climate reanalysis in the

0.25° grid cell containing DYE-2 indicate a similar summer temperature history, with a slightly negative but statistically insignificant trend. This result is echoed in the modelled melt, with no significant trend and a mean value of 0.14 ± 0.13 mm w.e. from 1997-2018 (Figure 8b). The interannual variability in summer melt is dominated by the exceptional summer of 2012, with a modelled melt of 0.64 m w.e., about 4σ above normal. The summer of 2012 was also exceptional with respect to meltwater infiltration (Figure 8d and Figure 9). The average depth of the summer meltwater infiltration and thaw fronts are 1.7 ± 1.4 m and 1.4 ± 1.4 m, respectively, with temperate conditions and meltwater infiltration confined to the upper 2 m of snow and firn in most years. The 2012 wetting and thaw fronts reached depths of 7.2 and 6.8 m, respectively: again, about 4σ above the normal.

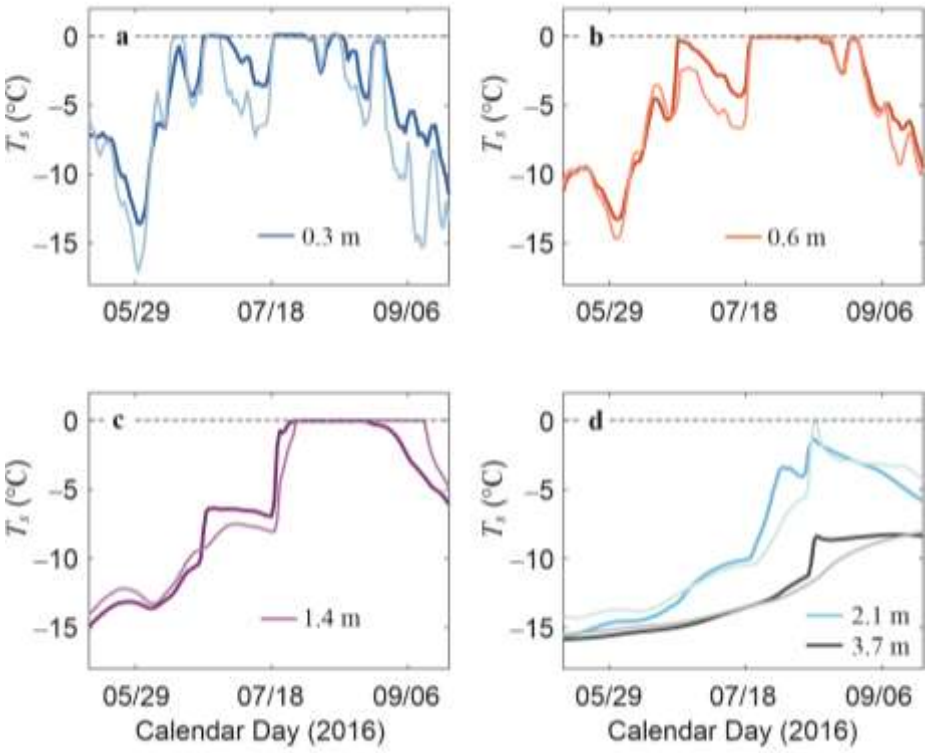

Figure 7. Observed (heavy lines, Site A) vs. modelled (light lines) mean daily snow/firn temperature through the summer melt season at depths of (a) 0.3 m, (b) 0.6 m, (c) 1.4 m, and (d) 2.1 and 3.7 m. Results are from a simulation with the optimized model parameters (see the text).

Mean annual air temperature also has no trend at DYE-2 over the period of GC-Net data, 1997-2018, but 10-m and 20-m firn temperatures (Figure 8c) do increase over this period, with statistically significant trends of +0.7 and +0.8°C per decade, respectively. The mean air

884 temperature at the GC-Net station is −17.6 ± 1.2°C, while the firn model predicts mean annual
885 temperatures of −16.3 ± 1.0°C and −16.3 ± 0.8°C at 10- and 20-m depth. Changes at 20 m lag
886 those at 10 m by about one year. On average, latent heat release warms the firn at DYE-2 by
887 about 1.3°C above the mean annual air temperature. The exceptional 2012 melt season caused a
888 warming of ~4°C at 10-m depth over the period 2012 to 2015 (Figures 8c and 9b), but the firn
889 recovered from this by 2018, with 10-m temperatures returning to −16.1°C. Figure 9c plots the
890 envelope of firn temperatures as a function of depth over the 22-year simulation, calculated from
891 the mean daily temperatures. The maximum envelope illustrates the temperate firn development
892 to 6.8 m depth in 2012, while the red dashed line, from 2016, represents a more typical summer.
893

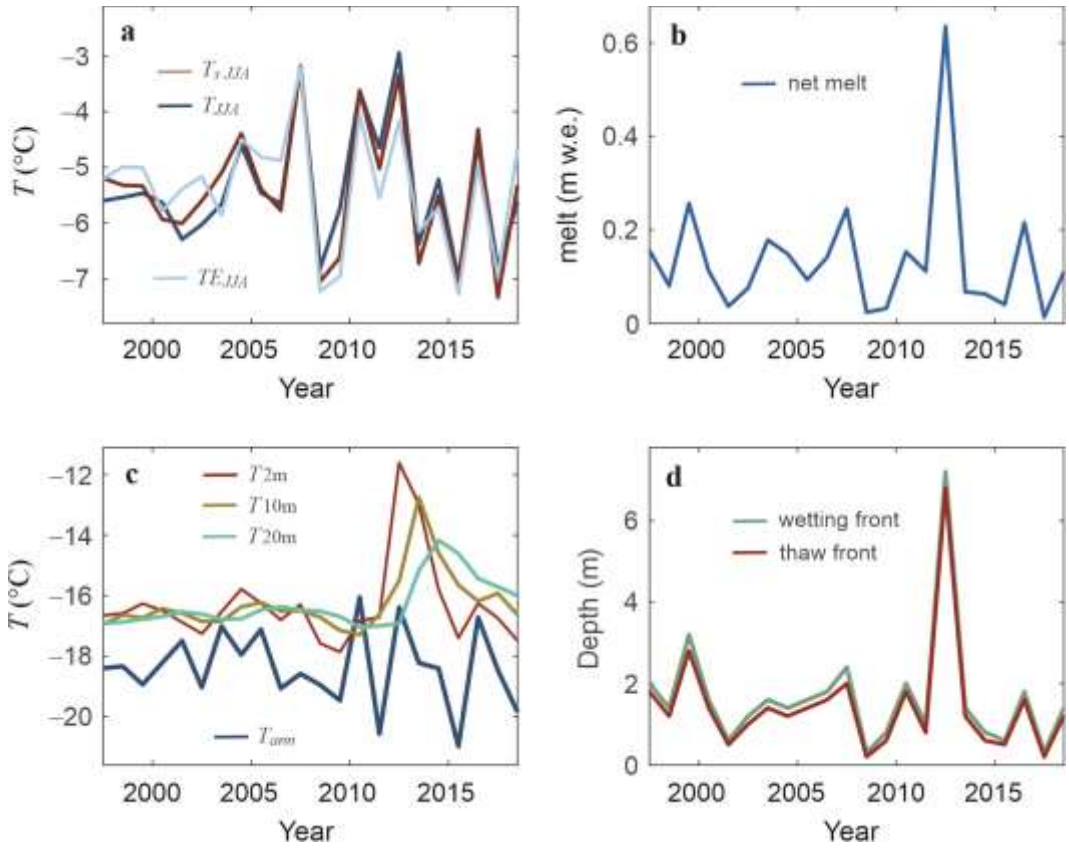

894
895
896 **Figure 8.** Modelled firn evolution at DYE-2, 1997-2018, forced by the GC-Net AWS data at this site. (a) Summer
897 (JJA) air and snow-surface temperatures. The light blue lines plot ERA5 mean JJA air temperatures, for comparison
898 with the GC-Net data. (b) Net annual surface melt. (c) Mean annual air temperature and firn temperatures at 5-, 10-
899 and 20-m depths. (d) Maximum depth of the annual wetting front and thaw front (0°C isotherm).
900

901 Measurements from the firn cores provide some validation of the modelled firn density and ice
902 content in the GC-Net-driven simulations. Examining the modelled 20-m firn profile in 2016, the

903 year of firn-core acquisition, the mean firn density and total ice content in the model are 6.1 m
904 and 693 kg m^{-3}. These are within 5% of the measured values in the 20.3-m firn core, a total ice
905 content of 6.4 m and a mean density of 665 kg m^{-3}. While these values agree within the
906 uncertainties of the measurements and the modelling, background firn density (i.e., firn
907 densification from Eq. 4) may be overestimated in the model, since bulk density is too high even
908 with a 5% underestimate in ice content.
909

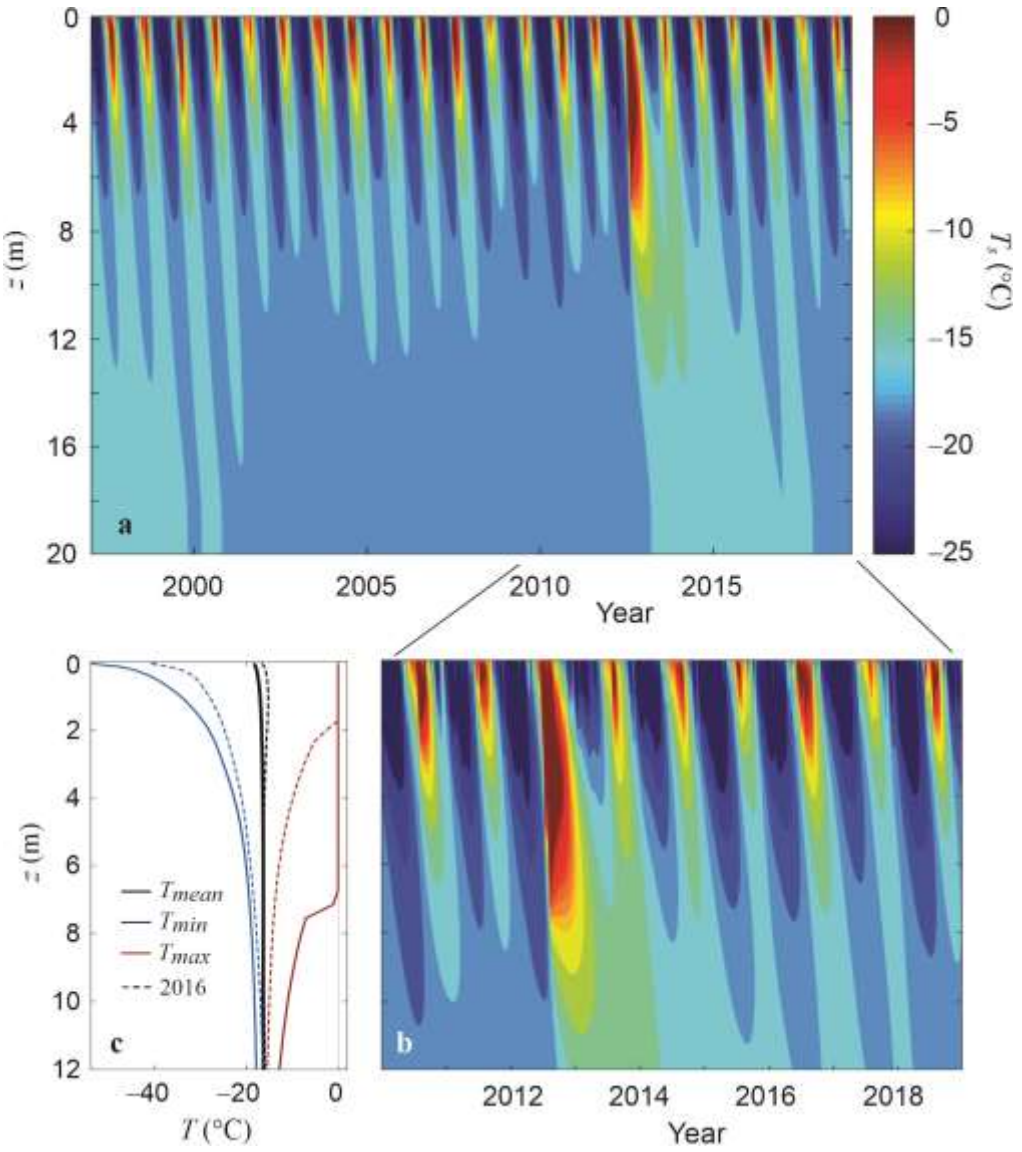

910
911

912 **Figure 9.** (a) Subsurface temperature evolution in the 20-m firn layer, 1997-2018. (b) Close-up of the upper 12 m of
913 firn from 2010-2018, highlighting the anomalous 2012 melt season. (c) Mean, minimum, and maximum mean daily
914 temperatures in the upper 12 m of snow and firn. Solid lines are for the entire period, 1997-2018, and dashed values
915 are for calendar year 2016, which is a typical year for this period.

ERA5 climate reanalyses provide a longer-term perspective on firn evolution at DYE-2. Modelled air temperatures, firn temperatures, and melt conditions from 1950-2020 are plotted in Figures 10 and 11. The average summer net melt over this 71-year period is 0.16 ± 0.12 m w.e., with average meltwater infiltration and thaw depths of 1.9 ± 1.3 m and 1.6 ± 1.3 m, respectively (Table 5). Average GC-Net and ERA5 results are similar over the common period in the simulations, 1997 to 2018 (Table 5), but there are some interannual differences. The 2012 extreme melt event was also extreme in the ERA5-forced model results, but is slightly muted relative to the GC-Net-driven simulations. Mean summer temperature in summer 2012 is lower in the ERA5 forcing relative to the GC-Net data, –4.2°C vs. –2.9°C (Table 5). This contributes to lower modelled melt totals, but the ERA-driven meltwater infiltration depth in 2012 still extends to 6 m depth, warming 10-m firn temperatures by 2.6°C.

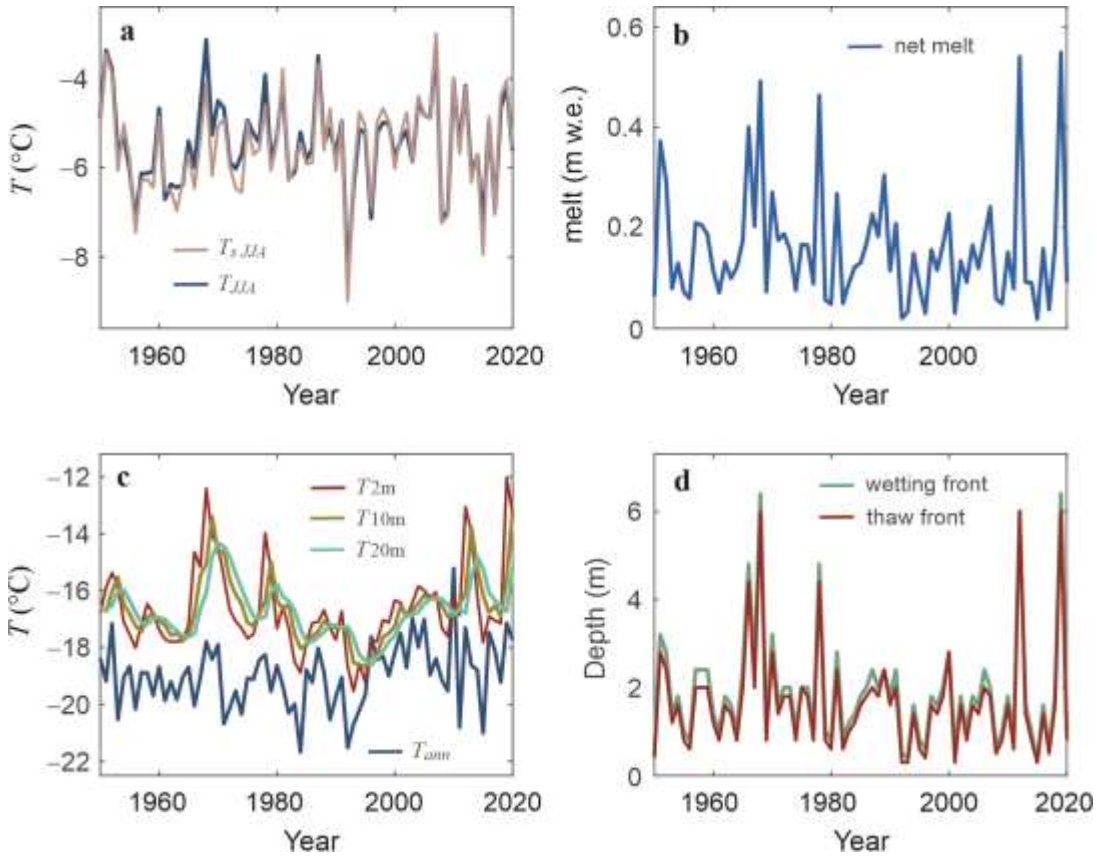

Figure 10. Modelled firn evolution at DYE-2, 1950-2020, forced by bias-adjusted ERA5 climate reanalyses. (a) Summer (JJA) air and snow-surface temperatures. (b) Net annual surface melt. (c) Mean annual air and firn temperatures at 5-, 10- and 20-m depths. (d) Maximum depth of the annual wetting and thaw fronts.

Table 5: Summer (JJA) climate, surface energy balance, and firn conditions at DYE-2 from 1950 to 2020, based on firn modelling forced by the ERA5 meteorological reanalyses. A subset of the results is shown for the period 1997-2018, for modelling driven by ERA5[E] and GC-Net[G] AWS data, as well as the extreme 2012 melt year. Melt refers to the total annual surface melting and 'net melt' refers to the net surface melting minus refreezing, accounting for meltwater freeze-thaw cycles. This is the actual surface drawdown associated with summer melting. All energy fluxes have units W m^{-2}, temperatures are in °C, PDD has units °C d, melt is in m w.e., and the thaw depth is in m.

Period	$Q_S^{\downarrow}$	Q^*	Q_H	Q_E	Q_N	T_a	T_{JJA}	*PDD*	*melt*	*net melt*	T_{10}	z_{thaw}
1950-2020[E]	307	15	4	–13	6	–18.0	–5.4	18.0	0.26	0.16	–16.7	1.6
1997-2018[E]	306	16	3	–14	5	–17.5	–5.4	14.3	0.24	0.14	–16.6	1.5
1997-2018[G]	306	16	2	–14	5	–17.6	–5.4	11.0	0.23	0.14	–16.3	1.4
2012[E]	304	26	5	–11	21	–16.5	–4.2	45.4	0.66	0.54	–13.8	6.0
2012[G]	298	30	7	–14	24	–15.6	–2.9	39.8	0.79	0.64	–12.8	6.8

There is a statistically significant trend in mean annual air temperature over the ERA5 period, +0.14°C per decade, but mean summer air temperature, firn temperatures annual melt, and meltwater infiltration depth have no trend over the full period, 1950-2020 (Figure 10). In contrast, there are significant positive trends over the more recent period 1990-2020. Summer (JJA) and mean annual air temperatures have trends of +0.19 and +0.50°C per decade over this period, net melt increased by +0.03 m w.e. per decade, and meltwater infiltration depth increased by +0.33 m per decade. These combined influences produced a statistically significant trend of +1.0°C per decade in 10-m firn temperatures, i.e., a 3°C increase over the last three decades. The firn warming is partially driven by the extreme melt years of 2012 and 2019, with more than 0.5 m w.e. of melting and meltwater infiltration to greater than 6 m depth in each of these summers (Figures 10b, 10d).

Deep meltwater infiltration events such as those of 2012 and 2019 are exceptional but are not isolated or unprecedented at DYE-2 in the ERA5-driven simulations. The summers of 1968 and 1978 featured similar summer temperatures, melt totals, and firn warming impacts (Figures 10, 11). The 1968 melt event resulted in a 10-m firn warming of ~4°C, exceeding the firn warming from 2012 (Figure 10c). The summer of 1968 was the warmest of the ERA5 period, with a mean JJA temperature of –3.1°C, and modelled meltwater infiltration reached 6.8 m in 1968. The strong impact on firn temperatures may have been aided by pre-conditioning from a strong melt season with meltwater infiltration to 4.8 m depth in 1966. The 2019 melt season was similar to that of 1968, with a predicted 10-m firn temperature anomaly of ~4°C that should still be present

at the time of writing. Within the model, the amount of seasonal meltwater is the primary driver of interannual variability in the depths of summer thaw and wetting fronts (Figures 9, 11). The linear correlation coefficient between net summer melt and meltwater infiltration depth is r = 0.97. Winter snow accumulation and temperature (i.e., snow and firn cold content) have some influence, but at DYE-2 there is still ample cold content and pore space to refreeze all of the summer meltwater, so seasonal meltwater infiltration depth is primarily a function of the amount of meltwater that is available as a latent heat source.

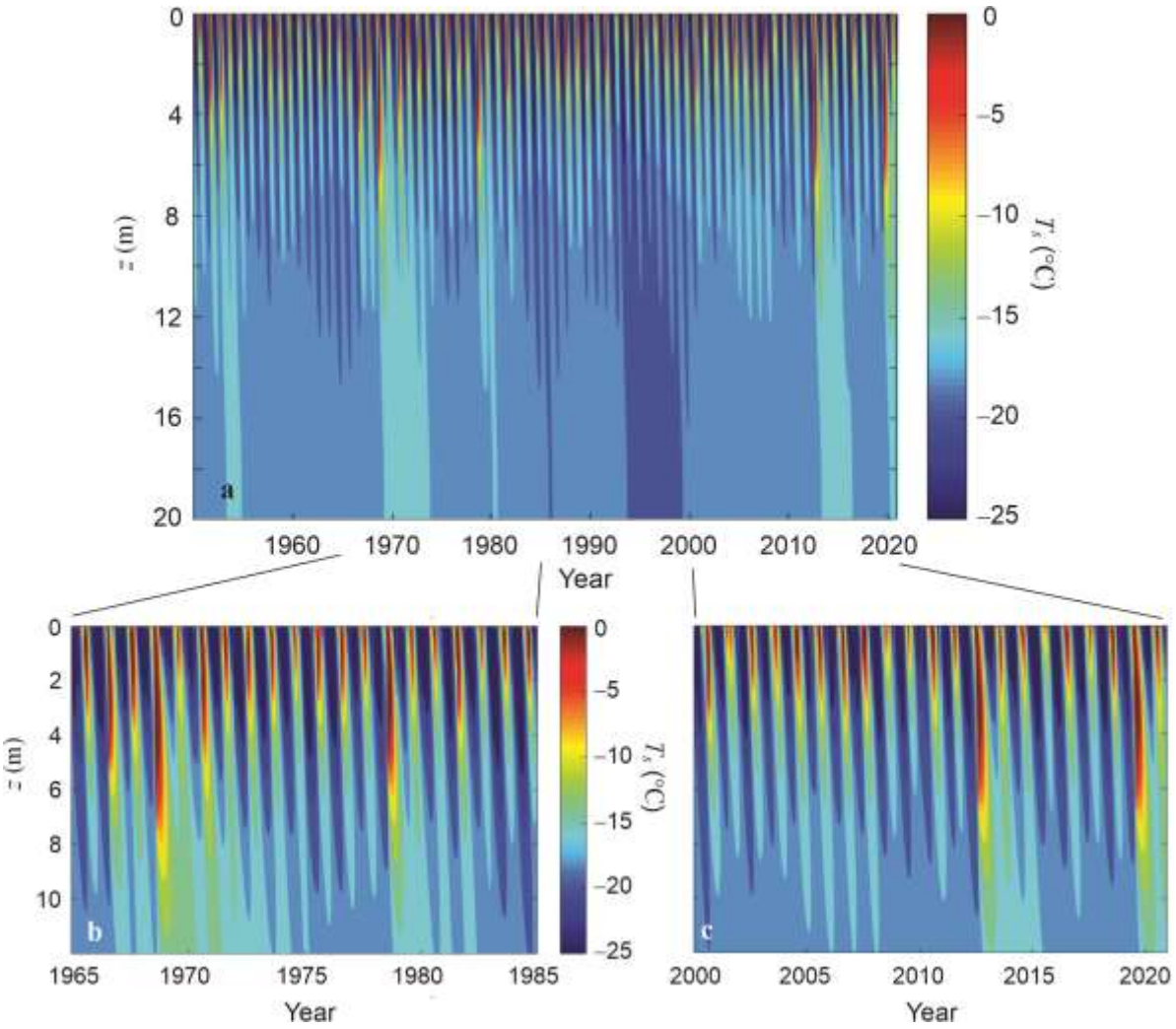

Figure 11. (a) Subsurface temperature evolution driven by ERA5 climate reanalyses in the 20-m firn layer, 1950-2020. (b) Close-up of the upper 12 m of firn from 1965-1985 and 2000-2020, highlighting the firn warming effects of meltwater infiltration to 6-7 m depth in 1968, 1978, 2012, and 2019.

4 Discussion

4.1 Assessment of TDR Methods in Polar Firn

4.1.1. TDR Precision and Accuracy

Prior to the onset of the melt season and over a time periods of weeks, where changes in density should be minimal, dielectric permittivity will be constant for dry snow and firn. This was true for dry conditions during the month of May at the study site. Bulk dielectric permittivity recorded by the TDR sensors had no trends at any depth, but was characterized by white noise with a standard deviation of 0.05 (i.e., a mean value for the eight probes at site B of $\varepsilon_b = 2.37 \pm 0.05$. This equates to a TDR-derived water content of $\theta_w = 0 \pm 0.03\%$. These dry-snow data provide an estimate of the instrumental precision in snow and firn, indicating that the sensors cannot reliably detect changes in liquid water content of less than ~0.5%. We infer typical liquid water contents of 1-2% under temperate conditions at DYE-2, with maximum values reaching ~5% (Figures 3 and 4), so the signal to noise ratio is adequate to detect wet snow and track meltwater pulses with depth. Low liquid-water contents or trace melt events are more challenging to capture with the TDR probes.

As an explicit example of the expected liquid water content at DYE-2, typical July melt rates at DYE-2 are 10 mm w.e. d^{-1} (Figure 2d), with peak hourly values of ~1 mm w.e. hr^{-1}. Over an hour, this equates to 1% by volume in the 0.1-m surface layer, so is detectable by the TDR sensors but not with high accuracy with respect to the amount of water. Once water content exceeds the capillary water retention capacity, water percolates vertically with high efficiency in temperate snow; the TDR records indicate that surface melt can infiltrate to depths of 0.5 m or more within the same day (Figures 3c,f). A total of 10 mm w.e. of daily melt distributed over the upper 0.5 m of snow is equivalent to 2% by volume. This is consistent with the inferred liquid water contents of 1-2% at DYE-2, and supports the promise for TDR methods in tracking meltwater infiltration in polar snow and firn.

4.1.2. Comparison with GPR Measurements

Continuous upward-looking GPR measurements from DYE-2 provide an independent estimate of meltwater infiltration during the 2016 melt season (Heilig et al., 2018). The timing and pattern

of meltwater evolution in the radar data reflects a similar step-wise evolution of the thawing and wetting fronts through the melt season, with a maximum meltwater infiltration depth on August 10 in both the TDR and radar records. The radar data indicate deeper infiltration than the TDR-based inferences, to 2.2 m vs. 1.8 m below the surface. Heilig et al. (2018) also infer maximum liquid water contents of ~2%, whereas the upper TDR sensors recorded values of up to 5% for short periods.

The differences between the two methods may be related to lateral variability in meltwater infiltration. Vertical sensor arrays cannot distinguish between the arrival of a uniform wetting front vs. preferential flow pathways, i.e., meltwater piping. The two firn pits instrumented with TDR sensors are consistent in the inference of wetting and thaw fronts to ~1.8 m depth, but the radar system may have detected a meltwater pipe that infiltrated to a greater depth. Given its burial depth of 4.3 m, the upward-looking GPR system of Heilig et al. (2018) monitored a cone with a horizontal footprint of ~70 m^2 at the surface. In contrast, the intrinsic horizontal resolution of the TDR measurements is the length of the TDR probes, 0.3 m. In sweeping over a larger volume of snow and firn, the radar data will integrate metre-scale variability in the meltwater infiltration. If there is significant lateral variability, averaging of water content over a given depth range in the radar data would give lower values for maximum water content, relative to the TDR measurements.

Broadly speaking, the two TDR arrays along with the radar data give similar results from three discrete points within a 400-m region at DYE-2. At each location, meltwater infiltration followed a similar evolution and reached a maximum depth of about 2 m in summer 2016. The question of spatial variability is an important one for meltwater infiltration and refreezing processes in firn (van As et al., 2016), and it is important to understand the extent and significance of lateral variability in meltwater infiltration for the evolution of firn temperature, stratigraphy, and density. This cannot be evaluated from our experimental design, but it would be possible to examine this though a more extensive sensor network that deploys horizontal as well as vertical sensor arrays. Such an approach is recommended for experiments to quantify local- to regional-scale lateral variability.

4.1.3. Dielectric Mixing Models

Mixing models to relate bulk dielectric permittivity to liquid water content in snow and firn are difficult to rigorously validate. Unlike in soils, where it is straightforward to evaporate off the liquid water and compare wet and dry masses, liquid water content in snow or firn is difficult to independently measure. The thermistor and TDR records during melt-freeze cycles provide some control on the TDR meltwater volume estimates. As an example, the abrupt subsurface warming to 0.5 m depth on June 22-23 (see Section 3.2) was driven by an estimated 13.6 mm w.e. of melt. Refreezing of 13.6 mm w.e. of meltwater would release 4.6×10^6 J of latent heat. The upper 0.5 m of snow had a mean density of ~340 kg m^{-3} and an average initial temperature of –4.2°C on June 22. Using a specific heat capacity of 2090 J kg^{-1} °C^{-1}, 1.5×10^6 J are needed to bring the upper 0.5 m of snow to the melting point, so the available meltwater/latent heat release readily accounts for this abrupt warming event. The cold content in the upper 0.5 of the snowpack is sufficient to refreeze about 33% of the available melt (4.5 mm w.e.), leaving 9.1 mm w.e. to be stored as liquid water, equivalent to an average liquid water content of 1.8% in the upper 0.5 m. The measured values of liquid water content in the upper 0.5 m averaged 1.7% for the period 08:00-20:00 on June 23 (Figures 4a,b), in good agreement with this estimate. We note that this is an open system, however, with conductive, sensible heat, and outgoing longwave radiation fluxes acting to transfer energy from the near-surface snowpack to the atmosphere through much of this period. This energy sink may have enabled more than 4.5 mm w.e. of meltwater to refreeze.

Different empirical equations have been used to estimate snow water content using dielectric and TDR methods (e.g., Denoth et al., 1984; Denoth, 1994; Schneebeli et al., 1997; Techel and Pielmeier, 2011). In lieu of empirical relations, mixing models in the general form of Eq. (2) have also been applied with different exponents in firn radar studies. Heilig et al. (2015, 2018) use an exponent $\beta = 0.5$ in a three-component mixing model, as described in detail in Schmid et al. (2014). Alternatively, numerous radar studies have adopted a mixing model after Looyenga (1965) with an exponent of 1/3 rather than 1/2 (e.g., Macheret et al., 1993; Murray et al., 2000; Christianson et al., 2015; Van Pelt et al., 2014). Samimi and Marshall (2017) found Eq. (3) with $\beta = 0.5$ to work well with TDR sensors in snow, based on validation against a Denoth (1994) capacitance plate and modelling of snow melt (hence, expected liquid water content). We

1079 therefore limit our experiments to this mixing model, which also permits a more direct
1080 comparison with the results of Heilig et al. (2018). The optimal mixing model may depend on the
1081 measurement technique, as instruments sample different length scales and orientations of the
1082 media. TDR probes sample a relatively small radius of influence, ca. 5 cm, in a two-dimensional
1083 sense, parallel to the surface and therefore within any horizontal layering. Effects of layering and
1084 anisotropic crystal orientation will therefore be minimal relative to the three-dimensional
1085 sounding that is intrinsic to radar wave propagation.
1086
1087 The empirical expression of Denoth (1994) relates snow dielectric permittivity to bulk density,
1088 ρ_b, and liquid water content following $\varepsilon_b = 1 + a_1 \rho_b + a_2 \rho_b^2 + a_3 \theta_w + a_4 \theta_w^2$, where a_1 =
1089 0.00192, $a_2 = 4.4 \times 10^{-7}$, $a_3 = 18.7$, $a_4 = 45$, and ρ_b has units kg m^{-3}. Estimates of liquid water
1090 content from Eq. (3) are less sensitive to changes in bulk dielectric permittivity than the equation
1091 of Denoth (1994). For reference values of $\theta_w = 0.02$ (2%) and $\rho_b = 500$ kg m^{-3}, the Denoth
1092 (1994) equation gives $\partial\theta_w/\partial\varepsilon_b = 0.049$ (4.9%) and the mixing model in our study gives $\partial\theta_w/\partial\varepsilon_b =$
1093 0.040 (4.0%). For a given measured increase in ε_b, estimates of θ_w from Eq. (3) are therefore
1094 about 20% less than would be inferred from the Denoth (1994) equations. Given this
1095 conservative estimate, the higher peak values of liquid water content in our data, compared with
1096 Heilig et al. (2018), are not likely to be an artefact of the mixing model.
1097
1098 *4.1.4. Effects of Changes in Snow and Firn Density*
1099 The dielectric permittivity of snow and firn increases with density as well as water content
1100 (Denoth et al., 1984; Schneebeli et al., 1997; Lundberg, 1997). An increase in snow density of
1101 100 kg m^{-3} is equivalent to a liquid water content of about 1% (Lundberg, 1997), so
1102 densification over the melt season may contribute to some of the bulk dielectric permittivity
1103 signal that we interpret as liquid water. We can assess the magnitude of this effect for dry firn
1104 densification for the two deepest TDR probes at site A. Firn at these depths remained frozen and
1105 unaffected by meltwater through the full 2016 melt season. These sensors recorded a gradual
1106 increase in dielectric permittivity over the melt season. Averaged over the period September 1-
1107 16, the end-of-summer values of ε_b increased above their May baseline values by $\Delta\varepsilon_b = +0.07$
1108 and $\Delta\varepsilon_b = +0.03$ at 2.8 and 3.7 m depth, respectively. In the mixing model for liquid water
1109 content (Eq. 3), this is equivalent to apparent liquid water contents of 0.29% and 0.12%, which is

less than the instrumental noise (0.5%).

Greater densification is expected near the surface in association with seasonal snow settling and refrozen meltwater. We partially account for these densification effects by resetting the reference dielectric permittivity for each TDR sensor after major refreezing cycles in the snow and firn, i.e., when θ_w drops to ~0 and temperatures fall below 0°C. Refrozen ice layers will increase the bulk density, but the baseline values of ε_b are renormalized for these effects. This restoration also eliminates the effects of potential changes in probe coupling with the snow and firn (e.g., air gaps) which may result from meltwater effects on the probes (e.g., Lundberg, 1997). Additional studies are needed to better understand the potential impacts of ice layer formation and freeze-thaw cycles on coupling of TDR probes and how this may affect the measured dielectric permittivity.

4.2 Surface Melt Estimates

We estimate a total summer melt of 0.18 ± 0.04 m w.e. based on the snow-surface height and density data at our two firn pits and estimates of snow densification. Energy balance modelling for the summer 2016 melt season gives 0.16 m w.e. with the reference model and 0.21 m w.e. of melt with the CLp7 parameter settings, which give a better fit to the observed meltwater infiltration and firn temperatures. For the CLp7 model, 74% of meltwater refreezes in the seasonal snow (0.16 m w.e.) and 26% (0.05 m w.e.) refreezes in the underlying firn, from 0.8 to 2 m depth below the surface. Heilig et al. (2018) estimate a total summer melt of 0.15 m w.e. in summer 2016, with 60% of the meltwater (0.09 m w.e.) refreezing in the seasonal snowpack and 40% (0.06 m w.e.) percolating into the underlying firn. Our melt values are higher than those of Heilig et al. (2018), but the estimates of infiltration and refreezing in the firn agree well.

Changes in near-surface firn ice content from 2016 to 2017 provide an independent estimate of the total melt in summer 2016. Firn cores were acquired each April and were logged at 5-cm intervals for density and ice layers. There is lateral variability in meltwater infiltration and refreezing on scales of 1 m (e.g., Dunse et al., 2008), which makes it difficult to compare the detailed stratigraphy of firn cores from different locations or years. Changes in total ice content in the upper firn column over one year never-theless provide an independent estimate of summer

meltwater. The TDR and thermistor records indicate that the summer 2016 thaw front reached a depth of 1.8 m at our sites. In April, 2016 (before the onset of melt), the upper 1.8 m of the firn core at Site A had a total ice content of 0.15 ± 0.02 m. Based on the snow-surface height data (Figure 2b), ablation in summer 2016 reduced this ~1.8 m of snow and firn to a layer ~1.55 m thick. When we acquired a new firn core at this site in April, 2017, 0.84 m of fresh snow had accumulated on the 2016 summer melt surface. The upper 2.4 m of this core (0.84 m of fresh snow and 1.56 m of firn) contained 0.35 ± 0.04 m of ice, indicating an increase in ice content of 0.2 ± 0.04 m over the year, or 0.18 ± 0.04 m w.e. Within uncertainties, this agrees with our melt estimates from the UDG records and both the reference and CLp7 models. This assessment assumes that all melt from summer 2016 refroze in visible ice layers, which may not be the case for capillary water that refreezes within the pore space. There may be some refrozen meltwater that we don't detect due to this, so estimates of total summer melt based on the ice stratigraphy represent a lower bound.

Firn cores at DYE-2 also provide longer-term context for the 2016 observations and the firn modelling from 1997-2018. The 20.3-m core acquired in 2016 had a total ice content of 6.4 m and an average density of 665 kg m^{-3}, giving an estimated total of 13.5 m w.e. Assuming an average accumulation rate of 0.36 m w.e. yr^{-1} (Mosley-Thompson et al., 2002), this represents ~38 years of accumulation, representing the period 1978-2016. If all of the annual meltwater refreezes somewhere in the firn column (i.e., assuming there is no runoff from the site), the 6.4 m of total ice content equates to an average melt/refreeze rate of 0.15 m w.e. yr^{-1}. Similar to the argument above, this estimate represents a lower bound as it only accounts for the visible ice layers and lenses identified in the core stratigraphy. Modelled melt rates forced by the GC-Net climatology average 0.14 m w.e. yr^{-1} from 1997 to 2018 (Table 5). These values are consistent with the expectations from the observed firn-core ice extent, although the time periods differ. Modelled melt rates with the ERA5 forcing are similar, with mean values of 0.14 m w.e. yr^{-1} from 1978-2016 and 0.16 m w.e. yr^{-1} from 1950-2020 (Table 5).

4.3 Firn Hydrology at DYE-2

4.3.1 Meltwater Infiltration

The observed meltwater infiltration depth in summer 2016, 1.8 m, is similar to the mean

maximum meltwater infiltration depth in the ERA5-forced model run, 1.9 ± 1.3 m. The summer 2016 melt season therefore appears to have been relatively normal for the period 1950-2020, and slightly above average for the GC-Net period, 1997-2018 (Table 5). Given the average accumulation rate of 0.36 m w.e. yr^{-1}, this means that summer meltwater at DYE-2 typically infiltrates the seasonal snow and firn from the previous 2 to 3 years, with 100% of the surface melt retained through refreezing. In heavy melt seasons such as 2012 and 2019, we model meltwater infiltration to depths of 6 to 7 m in the firn, through 10-12 years of net accumulation.

The TDR data and model experiments allow a closer analysis of meltwater infiltration and firn hydrological processes at DYE-2. There were four marked abrupt warming/latent heat release events in the 2016 melt season, on June 10-11, June 22-23, July 19-20, and August 9-11 (Figure 3). Average modelled melt rates on these days were 10.0 mm w.e. d^{-1}, compared with a JJA average of 2.2 mm w.e. d^{-1}. Meltwater was confined to the upper ~0.3 m of the snowpack in the first of these events, with each subsequent event propagating deeper into the firn. Subsurface warming in each case was associated with high production of meltwater and limited near-surface refreezing, which drove meltwater infiltration. On average for the summer, 49% of total meltwater refroze in the near-surface (the upper 0.2 m), but near-surface refreezing fell to 14% during the four melt events. The July 19-20 even was particularly strong, with average melt rates of 17.0 mm w.e. d^{-1} but none of this meltwater refreezing in the near-surface (i.e., 100% percolating to below 0.2 m depth).

Meltwater infiltration can be limited by ice layers, if these are able to act as low-permeability barriers to gravitational drainage (e.g., Bezeau et al., 2013; MacFerrin et al., 2019). Samimi et al. (2020) reported effective meltwater penetration through continuous ice layers up to 0.12 m thick at DYE-2 in summer 2016. No ice layers were thicker than this in the upper 2 m of the snow and firn in summer 2016, so we cannot assess the effective permeability of thick ice slabs, which are common at lower elevations in the Greenland percolation zone (MacFerrin et al., 2019). The 0.12-m ice layer was located from 0.96 to 1.08 m depth at site B, and we instrumented this firn pit immediately above and below this layer. Temperatures below 1.1 m remained sub-zero until the last major meltwater infiltration event on August 9, at which point the entire snow/firn column at site B developed wet, temperate conditions (Figure 3e). Average water content from

1.1 to 1.6 m depth increased from 0.5% on August 7-8 to 1.6% from August 9-12. The ice layer may have limited meltwater percolation prior to August 9, helping to maintain frozen conditions in the underlying firn. Alternatively, this may have been due to limited meltwater supply. Average modelled melt rates from July 21 to August 8 were 3.8 mm w.e. d^{-1}, then tripled to 11.0 mm w.e. d^{-1} from August 9-11. This final meltwater pulse provided sufficient latent heat to thaw the firn below 1 m, supporting the hydrological breakthrough to ~1.8 m.

4.3.2 Percolation Velocity

The percolation velocity or effective hydraulic conductivity, k_w (Eq. 13) can be characterized from the speed of infiltration during the four main meltwater pulses. As an example, the subsurface warming event on June 22-23, described in Section 4.1.3, involved meltwater infiltration to 0.5 m depth over a period of ~12 hours, indicating a meltwater percolation velocity of order 10^{-5} m s^{-1}. There is evidence for k_w values of up to ~10^{-4} m s^{-1} in some instances, e.g., meltwater percolating 0.3 m within one hour at site A. During the same melt event at site B, it required ~14 hours for meltwater to infiltrate to 0.4 m depth ($k_w = 8 \times 10^{-6}$ m s^{-1}). An analysis of meltwater arrival times at the TDR probes during all of the infiltration/abrupt warming events gives a range of between 1.5 and 12 hours for the meltwater to travel 0.2 to 0.4 m distance between probes in the upper 1.8 m of each pit. The equates to percolation velocities from 5×10^{-6} to 8×10^{-5} m s^{-1}. The lowest value, 5×10^{-6} m s^{-1}, corresponds to meltwater transmission through the 0.12-m thick ice layer at site B. The TDR sensor at 1.1 m depth first registered meltwater at 03:00 on July 20, 12 hours after it was first detected by the TDR sensor at 0.9 m depth, although liquid water content at and below 1.1 depth remained low until the August 9 meltwater pulse.

Differences in the values may be due to a combination of factors, including preferential flow pathways and delays associated with wetting and thawing of the snow and firn. The initial pulse of meltwater is held through capillary water retention before additional meltwater can drain. Meltwater percolation at DYE-2 also hits a thermal barrier to penetration before it can infiltrate to greater depths, i.e., limits to infiltration associated with refreezing in cold snow and firn. The thermal and wetting fronts co-developed in summer 2016 at DYE-2, so the effective hydraulic conductivity implicitly includes delays due to the effects of both capillary water retention and

meltwater refreezing. Once the near-surface snow was temperate through the main melt season from mid-July to mid-August, there is no evidence of diurnal cycles in liquid water content. This indicates that once snow is wetted and temperate, meltwater may be able to drain as quickly as it is produced at DYE-2. Maximum modelled daily melt rates in summer 2016 are 2×10^{-4} m s^{-1}.

4.3.4 Model Sensitivity to Hydrological Parameters

Model results are insensitive to changes in our reference value of the effective hydraulic conductivity between 10^{-3} and 10^{-7} m s^{-1}, bracketing the range of values inferred from the observations. This indicates that k_w is not an important free parameter in the model for the conditions at DYE-2, as long as delays associated with capillary water retention and thermal barriers to infiltration are accounted for. In contrast, modelled meltwater infiltration depths are highly sensitive to the treatment of irreducible water content, θ_{wi} (Figure 6), as identified in previous studies (Reijmer et al., 2012; Verjans et al., 2019). Higher values of capillary water retention reduce meltwater infiltration into the firn and reduce the net melt, since meltwater that is retained near the surface experiences multiple freeze-thaw cycles during the summer melt season. Our reference model values of θ_{wi} are typical of the irreducible water content reported in snow hydrology studies, about 3% by volume (Colbeck, 1974, Coléou and Lesaffre, 1998), although our optimized models have values closer to 2%. Accurate quantification of capillary water retention and its interaction with preferential infiltration pathways require further constraint in firn models. Targeted TDR experiments in polar snow and firn could help to examine this.

4.4 Meteorological Conditions During the Melt Events

Almost half of the total melt in summer 2016 was generated during the nine days represented by the four main melt events. These days were characterized by warm temperatures (average of –0.4°C, vs. a JJA average of –4.6°C) with minimal overnight cooling (Figure 2a). The net radiation, sensible heat flux, and latent heat flux were all above average during these events, giving an average net energy, Q_N, of 40 Wm^{-2}, compared with a JJA mean of 5 Wm^{-2}. This was driven by high values of incoming longwave radiation, $Q_L^{\downarrow}$: an average of 292 Wm^{-2}, compared with the mean JJA value of 240 Wm^{-2}. Incoming shortwave radiation was anomalously low during these events, indicative of overcast conditions that maintained high values of $Q_L^{\downarrow}$ for a

period of two to three days during each melt event, suppressing overnight refreezing. The continuous supply of meltwater and the suppression of near-surface cooling/refreezing facilitated the meltwater infiltration and firn warming events. The regional-scale meteorological control of these events is consistent with the similar, step-wise temporal evolution of meltwater infiltration and subsurface warming seen at our two pits and at the radar site.

4.5 Long-Term Firn Evolution at DYE-2

Decadal-scale firn warming is expected in Greenland in response to increases in air temperature and summer melting since the 1990s, which have driven strong reductions in surface mass balance (Mouginot et al., 2019; Shepherd et al., 2020; Hanna et al., 2021). Steffen and Box (2001) report a 10-m firn temperature of –16.5°C at DYE-2, representative of the period 1997-2000. GC-Net stations monitored firn temperatures to ~10 m depth until ~2010, and these records indicate a ~1°C warming of 10-m temperatures at DYE-2 from 1998 to 2009 (Vandecrux et al., 2020a). GC-Net firn temperature observations at DYE-2 were discontinued after 2010, so there are limited observations of firn temperatures in the last decade. Firn modelling by Vandecrux et al. (2020a) indicates a continuation of the observed warming trend for 10-m firn temperatures at DYE-2, with an overall trend of +1.1°C per decade for the period 1998-2017 and a 2017 value of about –15°C.

We attain an average modelled 10-m firn temperature of –16.3 ± 1.0°C for the period 1997-2018 with the GC-Net meteorological forcing, about 1°C cooler than the GC-Net observations and the estimate of Vandecrux et al. (2020a) for the latter part of this period. Trends in modelled 10-m and 20-m firn temperatures equal +0.7 and +0.8°C per decade for the period 1997-2018 (Figure 8c). These are statistically significant and are present despite the lack of a significant trend in surface air temperature or meltwater production over this period. The ERA5-forced results over the same period are also significant, with a 10-m temperature trend of +0.7°C per decade (Figure 10c). This increases to +1.0 °C per decade for the period 1997-2020, due to the influence of the 2019 extreme melt season.

The time series is short for evaluation of temporal trends at DYE-2 and results are sensitive to initial conditions (the model spin-up) and the precise time window. The latter is important due to

the large interannual variability; the positive trend in the model is partly due to the strong melt seasons of 2012 and 2019, which caused warm anomalies of 3-4°C at 10-m depth. Firn temperatures at 10- and 20-m depth fluctuate with time as a consequence of latent heat release, in contrast to a purely conductive environment where 10-m temperatures are representative of the mean annual surface temperature. In our modelling, the 10-m firn temperature reaches a maximum value of −12.8°C in early 2013 (Figure 8c), in response to the latent heat release from refreezing of the summer 2012 meltwater. A series of moderate melt seasons from 2013 to 2018 allowed 10-m temperatures to regress towards their 1997-2018 mean. Vandecrux et al. (2020a) also documented the transient excursion associated with the 2012 melt event at DYE-2, with a temporary loss of firn cold content but a restoration to more normal conditions by 2017. Firn temperature evolution at DYE-2 over the last two decades is dominated by the extreme 2012 and 2019 melt seasons, which strongly influence the 10-m temperature trend.

Temperature records from coastal and ice-sheet stations indicate a warming trend in Greenland from 1991-2018, but there is no significant temperature trend over the period 2001-2019 (Hanna et al., 2021). Warming in the early 2000s is offset by several cooler years in the period 2013-2018. The model results forced by GC-Net and ERA5 data are consistent with this, with significant increases in air and firn temperatures since 1990 but no trends in air temperature or modelled surface melt in the GC-Net period, 1997-2018. The extreme melt seasons of 2019 and 2012 are interesting anomalies within this period of relative climate stability at DYE-2. These years featured two of the three deepest meltwater infiltration events of at DYE-2 since 1950 (Figures 10 and 11), with 6 to 7 m of meltwater infiltration during these events. Strong melt seasons with similar impacts on 10-m firn temperatures also occurred in 1966, 1968, and 1978, with modelled meltwater infiltration and firn warming in 1968 exceeding that of 2012. Intermittent heavy melt seasons that cause transient firn warming are therefore not historically unprecedented. It requires several years for firn temperatures to recover from such events, however, so there are strong cumulative impacts from two such events in the last decade.

5 Conclusions

Vertical arrays of TDR probes show promise as a method to directly track the wetting front in

firn, enabling continuous monitoring of meltwater infiltration and refreezing processes along with estimates of firn water content. When combined with thermistors, these provide a coherent picture of the coupled firn hydrological and thermodynamic processes at DYE-2. The thaw and wetting fronts at DYE-2 advanced in tandem through a step-wise process in summer 2016, associated with four main pulses of meltwater and latent heat release (Figure 3). Meltwater infiltration drove the depth and timing of thaw front propagation through the summer melt season. The melt-season evolution was very similar at our two measurement sites, with a maximum wetting-front advance to 1.8 m depth in the second week of August at each site. The timing of detected meltwater infiltration events is in good accord with the upward-looking radar observations of Heilig et al. (2018), but we do not see evidence of wet or temperate firn below 1.8 m, while Heilig et al. (2018) detect liquid water to 2.3 m depth. The difference could be due to lateral variability in meltwater infiltration; the radar system has a larger spatial footprint than the TDR probes and may have detected preferential flow pathways within its footprint.

A model of the coupled thermodynamic and hydrological evolution gives a good representation of the meltwater infiltration, refreezing, and subsurface temperature evolution in the upper 4 m of snow and firn through the summer 2016 melt season (Figure 5). Meltwater infiltration and firn temperatures are slightly underestimated with the reference model settings for effective hydraulic conductivity and irreducible water content, with the latter based on Coléou and Lesaffre (1998). Results are very sensitive to the latter, and numerical experiments with reductions in irreducible water content provide improved fits to observed subsurface temperature and liquid water content. With reduced capillary water retention, less meltwater is retained in the surface layers and deeper infiltration increases the latent heat release in the firn. Our parameterization of meltwater infiltration is simplistic, lacking an explicit treatment of preferential flow (Wever et al., 2014; Verjans et al., 2019; Vandecrux et al., 2020b). As discussed by Verjans et al. (2019), reductions in capillary water retention could compensate for this. Additional model development, field, and lab experiments (e.g., Avanzi et al., 2016) are needed to better understand and quantify these processes in polar firn.

The observations of firn temperature, meltwater infiltration, and surface melt from summer 2016 were used to constrain our firn model. Simulations with the optimized model provide insight into

the longer-term firn evolution at DYE-2 over the period of record of GC-Net AWS data, 1997-2018, and over the multi-decadal timescale of ERA5 climate reanalyses, 1950-2020. There is a significant long-term warming signal at DYE-2 for mean annual temperatures, +0.14°C per decade, but summer (JJA) and firn temperatures show no significant long-term trends in the ERA5-forced reconstructions from 1950-2020. As seen in Greenland temperature records, however (Hanna et al., 2012, 2021), there are significant warming trends in recent decades. Modelled 10-m firn temperature at DYE-2 has a trend of +1.0°C per decade from 1990-2020. Annual and summer air temperature, melt rates, and meltwater infiltration depths all increased at DYE-2 since 1990, with an average depth of meltwater infiltration ($\pm 1\sigma$) of 1.7 ± 1.5 m and a trend of +0.33 m per decade from 1990-2020.

Firn temperature, ice content, and density at DYE-2 are strongly affected by extreme melt seasons such as 2012 and 2019. High melt extents in these two summers, about 4σ above normal, drove meltwater infiltration to depths of 6-7 m in the model, causing a 10-m firn warming of 3 to 4°C that persists for several years. Firn temperatures from 10-20 m depth were almost restored to their pre-2012 conditions when the 2019 melt event produced similar impacts. These events are rare but not unprecedented in the 71-year historical reconstruction at DYE-2; we model meltwater infiltration to 6.8 m depth in 1968, driving the strongest firn warming event of the last 71 years. This coincided with the warmest summer on record in the ERA5 reanalysis at DYE-2. Meltwater infiltration to ~5 m depth was also simulated in 1966 and 1978. Firn warming, densification, and ice content, and the associated implications for meltwater retention in the upper Greenland percolation zone may be more sensitive to the frequency of extreme melt seasons than the background climate warming trend.

Our model results are constrained by field observations in summer 2016, but we do not have observational constraints on the firn thermodynamic and hydrological evolution during an extreme melt season. More work is also needed to refine our model treatments of capillary water retention and preferential flow pathways, as discussed above; field data of the kind presented here could help to elucidate these processes. Studies lower in the percolation zone would help to examine the effects of greater meltwater production and thicker ice layers. Direct observations of surface melt rates would support this, to rigorously calibrate the surface energy balance model

and the model predictions of net vs. total melt. Two-dimensional networks of TDR probes and thermistors could provide insight into heterogeneity at local scales, but lateral variability of meltwater infiltration and refreezing processes on regional scales remains a large challenge in understanding and quantifying Greenland firn hydrology. Given the likely expansion of Greenland's percolation zone to higher elevations in the coming decades, realistic treatments of these processes will be increasingly important for projections of Greenland Ice Sheet surface mass balance and Greenland's contributions to global sea level rise.

Acknowledgments

We thank the FirnCover 2016 team for support in the field, including Liam Colgan, Aleah Sommers, Darren Hill, Achim Heilig, Bastian Gerling, and Leander Gambal. Research costs of SS and SJM were supported by the Natural Sciences and Engineering Research Council (NSERC) and ArcTrain Canada, and the FirnCover project was funded by the NASA Roses program, grant number NNX15AC62G. The U.S. National Science Foundation, Air National Guard, and CH2MHill Polar Field Services provided essential logistical support for this study.

The authors declare no personal, financial, or professional conflicts of interest with the results or conclusions of this study. Datasets from this study are available at Samimi and Marshall (2020), and the MATLAB code used for the firn modeling is available in a repository at Marshall (2021).

References

Avanzi, F., Hirashima, H., Yamaguchi, S., Katsushima, T. & De Michele, C. (2016). Observations of capillary barriers and preferential flow in layered snow during cold laboratory experiments. *The Cryosphere*, *10*, 2013–2026. https://doi.org/10.5194/tc-10-2013-2016.

Benson, C. S. (1962). *Stratigraphic Studies in the Snow and Firn of the Greenland Ice Sheet*. Research Report 70, SIPRE.

Bezeau, P., Sharp, M., Burgess, D. O. & Gascon, G. (2013). Firn profile changes in response to extreme 21st-century melting at Devon Ice Cap, Nunavut, Canada. *Journal of Glaciology*, *59*, 981–991. doi: 10.3189/2013JoG12J208.

1417 Birchak, J. R., Gardner, C. G., Hipp, J. E. & Victor, J. M. (1974). High dielectric constant microwave probes for
1418 sensing soil moisture. *Proc. IEEE, 62* (1), 93-98.

1419 Brown, J., Harper, J., Pfeffer, W. T., Humphrey, N. & Bradford, J. (2011). High-resolution study of layering within
1420 the percolation and soaked facies of the Greenland ice sheet. *Annals of Glaciology*, *52* (59), 35-42.

1421 Calonne, N., Milliancourt, L., Burr, A., Philip, A., Martin, C. L., Flin, F. & Geindreau, C. (2019). Thermal
1422 conductivity of snow, firn and porous ice from 3-D image-based computations. *Geophysical Research Letters*,
1423 *46* (22), 13,079-13,089, https://doi.org/10.1029/2019GL085228.

1424 Charalampidis, C., van As, D., Colgan, W. T., Fausto, R. S., MacFerrin, M. & Machguth, H. (2016). Thermal
1425 tracing of retained meltwater in the lower accumulation area of the southwestern Greenland ice sheet. *Annals of*
1426 *Glaciology*, 57, doi:10.1017/aog.2016.2.

1427 Clausen, H. B., Gundestrup, N. S., Johnsen, S. J., Bindschadler, R., & Zwally, J. (1988). Glaciological investigations
1428 in the Crête area, central Greenland: a search for a new deep-drilling site. *Annals of Glaciology*, *10*, 10–15,
1429 doi:10.3189/S0260305500004080.

1430 Colbeck, S. C. (1974). The capillary effects on water percolation in homogeneous snow. *Journal of Glaciology*, *13*
1431 (67), 85-97, doi:10.3189/S002214300002339X.

1432 Coléou, C. & Lesaffre, B. (1998). Irreducible water saturation in snow: experimental results in a cold
1433 laboratory. *Annals of Glaciology*, *26*, 64–68, https://doi.org/10.3189/1998AoG26-1-64-68.

1434 Cuffey, K. M. & Paterson, W. S. B. (2010). *The Physics of Glaciers, 4th Ed.* Academic Press, Burlington, MA.

1435 Denoth, A. (1994). An electronic device for long-term snow wetness recording. *Annals of Glaciology* 19, 104–106.

1436 Denoth, A., Foglar, A., Weiland, P., Matzler, C., Aebischer, H., Tiuri, M. & Sihvola, A. (1984). A comparative
1437 study of instruments for measuring the liquid water content of snow. *Journal of Applied Physics*, *56* (7), 2154–
1438 2160, doi:10.1063/1.334215.

1439 de la Peña, S., Howat, I. M., Nienow, P. W., van den Broeke, M. R., Mosley-Thompson, E., Price, S. F. et al. (2015).
1440 Changes in the firn structure of the western Greenland Ice Sheet caused by recent warming. *The Cryosphere*, *9*,
1441 1203–1211. doi: 10.5194/tc-9-1203-2015.

1442 Dunse, T., Eisen, O., Helm, V., Rack, W., Steinhage D. and Parry, V. (2008). Characteristics and small-scale
1443 variability of GPR signals and their relation to snow accumulation in Greenland's percolation zone. *Journal of*
1444 *Glaciology*, *54* (185), 333-342. doi:10.3189/002214308784886207.

1445 Ebrahimi, S. & Marshall, S. J. (2016). Surface energy balance sensitivity to meteorological variability on Haig
1446 Glacier, Canadian Rocky Mountains. *The Cryosphere*, *10*, 2799–2819, https://doi.org/10.5194/tc-10-2799-2016.

1447 Evans, S. (1965). Dielectric properties of ice and snow–a review. *Journal of Glaciology*, *5* (42), 773-792.
1448 doi:10.3189/S0022143000018840.

1449 Fettweis, X., Hanna, E., Lang, C., Belleflamme, A., Erpicum, M. & Gallée, H. (2013). Important role of the mid-
1450 tropospheric atmospheric circulation in the recent surface melt increase over the Greenland ice sheet. *The*
1451 *Cryosphere*, 7, 241–248. https://doi.org/10.5194/tc-7-241-2013.

1452 Gascon, G., Sharp, M., Burgess, D., Bezeau, P. & Bush, A. B. G. (2013). Changes in accumulation-area firn
1453 stratigraphy and meltwater flow during a period of climate warming: Devon Ice Cap, Nunavut,
1454 Canada. *Journal of Geophysical Research - Earth Surface*, *118*, 2380–2391. doi: 10.1002/2013jf002838.

1455 Hanna, E., Mernild, S. H., Cappelen, J. & K. Steffen, K. (2012). Recent warming in Greenland in a long-term
1456 instrumental (1881–2012) climatic context: I. Evaluation of surface air temperature records. *Environmental*
1457 *Research Letters*, *7*, 045404.

1458 Hanna, E., Fettweis, X., Mernild, S. H, Cappelen, J., Ribergaard, M. H., Shuman, C. A., Steffen, K., Wood, L. &
1459 Mote, T. L. (2014). Atmospheric and oceanic climate forcing of the exceptional Greenland ice sheet surface
1460 melt in summer 2012. *International Journal of Climatolology*, *34*, 1022–1037.

1461 Hanna, E., Cappelen, J., Fettweis, X., Mernild, S. H., Mote, T. L., Mottram, R., Steffen, K., Ballinger, T. J. & Hall,
1462 R. J. (2021). Greenland surface air temperature changes from 1981 to 2019 and implications for ice-sheet melt
1463 and mass-balance change. *International Journal of Climatolology*, *41* (S1), E1336-E1352,
1464 https://doi.org/10.1002/joc.6771.

1465 Harper, J., Humphrey, N., Pfeffer, W. T., Brown, J. & Fettweis, X. (2012). Greenland ice-sheet contribution to sea-
1466 level rise buffered by meltwater storage in firn. *Nature*, *491*, 240–243, doi: 10.1038/nature11566.

1467 Heilig A., Eisen, O., MacFerrin, M., Tedesco, M., & Fettweis, X. (2018). Seasonal monitoring of melt and
1468 accumulation within the deep percolation zone of the Greenland Ice Sheet and comparison with simulations of
1469 regional climate modeling. *The Cryosphere*, *12* (6), 1851–1866. doi: 10.5194/tc-12- 1851-2018.

1470 Hersbach, H., Bell, B., Berrisford, P. et al. (2020). The ERA5 global reanalysis. *Quarterly Journal of the Royal*
1471 *Meteorological Society*, *146* (730), 1999-2049. https://doi.org/10.1002/qj.3803.

1472 Hirashima, H., Yamaguchi, S., Sato, A. & Lehning, M. (2010). Numerical modeling of liquid water movement
1473 through layered snow based on new measurements of the water retention curve. *Cold Regions Science and*
1474 *Technology*, *64*, 94–103, doi: 10.1016/j.coldregions.2010.09.003.

1475 Humphrey, N. F., Harper, J. T. & Pfeffer, W. T. (2012). Thermal tracking of meltwater retention in Greenland's
1476 accumulation area. *Journal of Geophysical Research*, *117* (F01010), doi: 10.1029/2011JF002083.

1477 Katsushima, T., Yamaguchi, S., Kumakura, T., & Sato, A. (2013). Experimental analysis of preferential flow in dry
1478 snowpack. *Cold Regions Science and Technology*, *85*, 206-216, doi: 10.1016/j.coldregions.2012.09.012.

1479 Kuipers Munneke, P., Ligtenberg, S. R. M., Noël, B. P. Y., Howat, I. M., Box, J. E., Mosley-Thompson, E. et al.
1480 (2015). Elevation change of the Greenland Ice Sheet due to surface mass balance and firn processes, 1960–
1481 2014. *The Cryosphere*, *9*, 2009–2025, https://doi.org/10.5194/tc-9-2009-2015.

1482 Langen, P., Fausto, R. S., Vandecrux, B., Mottram, R. H. & Box, J. E. (2017). Liquid water flow and retention on
1483 the Greenland Ice Sheet in the regional climate model HIRHAM5: Local and large-scale impacts. *Frontiers in*
1484 *Earth Science*, *4* (110), https://doi.org/10.3389/feart.2016.00110.

1485 Lundberg, A. (1997). Lab calibration of TDR probes for snow-wetness measurements. *Cold Regions Science and*
1486 *Technology*, *25* (3), 197-205, https://doi.org/10.1016/S0165-232X(96)00012-2.

1487 MacFerrin, M., Machguth, H., van As, D., Charalampidis, C., Stevens, C. M., Heilig, A. et al. (2019). Rapid
1488 expansion of Greenland's low-permeability ice slabs. *Nature*, *573*, 403–407. https://doi.org/10.1038/s41586-
1489 019-1550-3.

1490 Machguth, H., MacFerrin, M., Van As, D., Box, J. E., Charalampidis, C., Colgan, W. et al. (2016). Greenland
1491 meltwater storage in firn limited by near-surface ice formation. *Nature Climate Change*, *6*, 390–393. doi:
1492 10.1038/nclimate2899.

1493 Marsh, P. & Woo, M.-K. (1984). Wetting front advance and freezing of meltwater within a snow cover. 2. A
1494 simulation model. *Water Resources Research*, *20*, 1865-187.

1495 Marshall, S. J. (2021). MATLAB code for firn thermodynamic and hydrological modelling. Scholars Portal
1496 Dataverse, V1, https://doi.org/10.5683/SP2/WRWJAZ.

1497 Mosley-Thompson, E., McConnell, J. R., Bales, R. C., Lin, P. N., Steffen, K., Thompson, L. G. et al. (2001). Local
1498 to regional-scale variability of annual net accumulation on the Greenland ice sheet from PARCA cores. *Journal*
1499 *of Geophysical Research*, *106*, 33839–33851. doi: 10.1029/2001JD900067.

1500 Mouginot, J., Rignot, E., Bjørk, A. A., van den Broeke, M. R., Millan, R., Morlighem, M., Noël, B., Scheuchl, B. &
1501 Wood, M. (2019). Forty-six years of Greenland Ice Sheet mass balance from 1972 to 2018. *Proceedings of the*
1502 *U.S. National Academy of Sciences*, *116* (19), 9239-9244, https://doi.org/10.1073/pnas.1904242116.

1503 Nghiem, S. V., Hall, D. K., Mote, T. L., Tedesco, M., Albert, M. R., Keegan, K., Shuman, C. A., DiGirolamo, N. E.
1504 & Neumann, G. (2012). The extreme melt across the Greenland ice sheet in 2012. *Geophysical Research*
1505 *Letters*, *39* (20), 2012GL053611. doi:10.1029/2012GL053611.

1506 Noël, B. B. Y., van de Berg, W. J., Lhermitte, S., Wouters, B., Machguth, H., Howat, I. et al. (2017). A tipping point
1507 in refreezing accelerates mass loss of Greenland's glaciers and ice caps, *Nature Communications*, *8*, 14730,
1508 https://doi.org/10.1038/ncomms14730.

1509 Parry, V., Nienow, P., Mair, D., Scott, J., Hubbard, B., Steffen, K. & Wingham, D. (2007). Investigations of
1510 meltwater refreezing and density variations in the snowpack and firn within the percolation zone of the
1511 Greenland ice sheet. *Annals of Glaciology*, *46*, 61-68, doi:10.3189/172756407782871332.

1512 Pfeffer, W. T. & Humphrey, N. F. (1998). Formation of ice layers by infiltration and refreezing of meltwater. *Annals*
1513 *of Glaciology* 26, 83-91.

1514 Reijmer, C. H., van den Broeke, M. R., Fettweis, X., Ettema, J. & Stap, L. B. (2012). Refreezing on the Greenland
1515 ice sheet: a comparison of parameterizations. *The Cryosphere*, *6*, 743–762. https://doi.org/10.5194/tc-6-743-
1516 2012.

1517 Roth, K., Schulin, R., Flühler, H. & Attinger, W. (1990). Calibration of time domain reflectometry for water content
1518 measurement using a composite dielectric approach. *Water Resources Research*, *26*, 226–273.

1519 Samimi, S. & Marshall, S. J. (2017). Diurnal cycles of meltwater percolation, refreezing, and drainage in the
1520 supraglacial snowpack of Haig Glacier, Canadian Rocky Mountains. *Frontiers in Earth Science*, *5*, 1–15,
1521 https://doi.org/10.3389/feart.2017.00006.

1522 Samimi, S. & Marshall, S. J. (2020). Meteorological and Firn data from DYE-2, Greenland Ice Sheet, Summer
1523 2016. Scholars Portal Dataverse, V1, https://doi.org/10.5683/SP2/2QY39K.

1524 Samimi, S., Marshall, S. J. & MacFerrin, M. (2020). Meltwater penetration through temperate ice layers in the
1525 percolation zone at DYE-2, Greenland Ice Sheet. *Geophysical Research Lett*ers, *47*, e2020GL089211.
1526 https://doi.org/10.1029/2020GL089211.

1527 Schmid, L., Heilig, A., Mitterer, C., Schweizer, J., Maurer, H., Okorn, R., & Eisen, O. (2014). Continuous snowpack
1528 monitoring using upward-looking ground-penetrating radar technology. *Journal of Glaciology*, *60* (221), 509–
1529 525. doi:10.3189/2014JoG13J084.

1530 Schneebeli, M., Coléou, C., Touvier, F. & Lesaffre, B. (1997). Measurement of density and wetness in snow using
1531 time-domain reflectometry. *Annals of Glaciology*, *26*, 69-72, doi:10.3189/1998aog26-1-69-72.

1532 Shepherd, A., Ivins, E., Rignot, E. & the IMBIE Team (2020). Mass balance of the Greenland Ice Sheet from 1992
1533 to 2018. *Nature*, *579*, 233–239, https://doi.org/10.1038/s41586-019-1855-2.

1534 Shoji, H., Clausen, H. B. & Kameda, T. (1991). Accumulation rate at Site-J and Dye-2, Greenland. *Bulletin of*
1535 *Glaciological Research*, *9*, 85-88.

1536 Sørensen, L. S., Simonsen, S. B., Nielsen, K., Lucas-Picher, P., Spada, G., Adalgeirsdottir, G., Forsberg, R. &
1537 Hvidberg, C. S. (2011). Mass balance of the Greenland ice sheet (2003–2008) from ICESat data – the impact of
1538 interpolation, sampling and firn density. *The Cryosphere*, *5*, 173–186, https://doi.org/10.5194/tc-5-173-2011.

1539 Steger, CR, Reijmer, CH, van den Broeke, MR, Wever, N, Forster, RR, Koenig, LS et al. (2017a) Firn meltwater
1540 retention on the Greenland Ice Sheet: A model comparison. *Frontiers in Earth Science* 5 (3),
1541 https://doi.org/10.3389/feart.2017.00003.

1542 Steger, CR, Reijmer, CH and van den Broeke, MR (2017b) The modelled liquid water balance of the Greenland Ice
1543 Sheet. *The Cryosphere* 11, 2507–2526, https://doi.org/10.5194/tc-11-2507-2017.

1544 Steffen, K and Box, JE (2001) Surface climatology of the Greenland ice sheet: Greenland climate network 1995-
1545 1999. *Journal of Geophysical Research - Atmospheres* 106 (D24), 33951–33964,
1546 https://doi.org/10.1029/2001JD900161.

1547 Techel, F and Pielmeier, C (2011) Point observations of liquid water content in wet snow–investigating methodical,
1548 spatial and temporal aspects. *The Cryosphere* 5, 405–418. doi: 10.5194/tc-5-405-2011.

1549 Tedesco, M and Fettweis, X (2020) Unprecedented atmospheric conditions (1948-2019) drive the 2019 exceptional
1550 melting season over the Greenland ice sheet. *The Cryosphere*, 14, 1209–1223.

1551 Tiuri, M, Sihvola, A, Nyfors, E and Hallikaiken M (1984) The complex dielectric constant of snow at microwave
1552 frequencies. *IEEE Journal of Oceanic Engineering*, 9, 377–382. doi: 10.1109/JOE.1984.1145645.

1553 van Angelen, JH, Lenaerts, JTM, van den Broeke, MR, Fettweis, X and van Meijgaard, E (2013) Rapid loss of firn
1554 pore space accelerates 21st century Greenland mass loss. *Geophysical Research Letters* 40, 2109–2113.
1555 https://doi.org/10.1002/grl.50490

1556 van As, D, Box, JE and Fausto, RS (2016) Challenges of quantifying meltwater retention in snow and firn: An
1557 expert elicitation. *Frontiers in Earth Science* 4 (101). doi: 10.3389/feart.2016.00101.

1558 Vandecrux, B, Fausto, RS, Langen, PL et al. (2018) Drivers of firn density on the Greenland ice sheet revealed by
1559 weather station observations and modeling. *Journal of Geophysical Research - Earth Surface* 123, 2563–2577,
1560 https://doi.org/10.1029/2017JF004597.

1561 Vandecrux, B., Fausto, R. S., van As, D. et al. (2020a). Firn cold content evolution at nine sites on the Greenland ice
1562 sheet between 1998 and 2017. *Journal of Glaciology*, *66*, 591–602. https://doi.org/10.1017/jog.2020.30.

1563 Vandecrux, B., Mottram, R., Langen, P. L., Fausto, R. S., Olesen, M., Stevens, C. M. et al. (2020b). The firn
1564 meltwater Retention Model Intercomparison Project (RetMIP): evaluation of nine firn models at four weather
1565 station sites on the Greenland ice sheet. *The Cryosphere*, *14*, 3785–3810, https://doi.org/10.5194/tc-14-3785-
1566 2020.

1567 Verjans, V., Leeson, A. A., Stevens, C. M., MacFerrin, M., Noël, B. & van den Broeke, M. R. (2019). Development
1568 of physically based liquid water schemes for Greenland firn-densification models, *The Cryosphere*, *13*, 1819–
1569 1842. https://doi.org/10.5194/tc-13-1819-2019.

1570 Vionnet, V., Brun, E., Morin, S., Boone, A., Faroux, S., Le Moigne, P. et al. (2012). The detailed snowpack scheme
1571 Crocus and its implementation in SURFEX v7.2. *Geoscience Model Development*, *5*, 773–791.
1572 doi:10.5194/gmd-5-773-2012.

1573 Wever, N., Fierz, C., Mitterer, C., Hirashima, H. & Lehning, M. (2014). Solving Richards Equation for snow
1574 improves snowpack meltwater runoff estimations in detailed multi-layer snowpack model, *The Cryosphere*, *8*,
1575 257–274, https://doi.org/10.5194/tc-8-257-2014.

1576 Williams, M. W., Erickson, T. A. & Petrzelka, J. L. (2010). Visualizing meltwater flow through snow at the
1577 centimetre-to-metre scale using a snow guillotine. *Hydrological. Processes*, *24*, 2098-2110.
1578 https://doi.org/10.1002/hyp.7630.

1579 Yamaguchi, S., Watanabe, K., Katsushima, T., Sato, A. & Kumakura, T. (2012). Dependence of the water retention
1580 curve of snow on snow characteristics. *Annals of Glaciology*, *53* (61), 6–12, doi:10.3189/2012AoG61A00.